

24 steel moment-resisting frames. The case studies show that the linear constraint equation formulation
25 may not be suitable for all problems, however, it may still yield acceptable results as long as the
26 level of twisting is insignificant and lateral-torsional buckling is not critical.

27 Keywords: Continuum finite element analysis; Steel structures; Nonlinear geometric instabili-
28 ties; Kinematic coupling; Beam-columns.

29 INTRODUCTION

30 Background

31 Simulation-based infrastructure design against natural hazards, such as earthquakes, relies
32 heavily on the development of representative models of various fidelities (Krawinkler et al. 2006).
33 Additionally, numerical models are necessary to evaluate the vulnerability of buildings and bridges
34 and the social vulnerability of populations in at-risk communities (Deierlein and Zsarnóczy 2019).
35 Within the scope of steel structures subjected to earthquake hazards, geometric instabilities are a
36 significant source of structural damage, therefore, modeling this effect is a necessity. Models that
37 simulate nonlinear geometric instabilities in steel structures under cyclic loading can be divided into
38 three main categories of increasing fidelity and complexity: (a) point hinge models (concentrated
39 plasticity); (b) distributed plasticity models (commonly using fiber beam-column elements); and
40 (c) continuum finite element (CFE) models. Although fracture can be critical for steel components,
41 the focus of this paper is mainly on models simulating component-level strength and stiffness
42 deterioration due to local and/or member instabilities (member and lateral torsional buckling), as
43 well as their interaction.

44 Point hinge models are placed at predefined locations of anticipated plasticity along a member.
45 Concentrated plasticity models are known to be computationally efficient for parametric nonlinear
46 analyses of metal structures (e.g., Ibarra and Krawinkler (2005)), and do not suffer from spurious
47 localization issues during component deterioration. Sivaselvan and Reinhorn (2000) and Ibarra
48 et al. (2005) proposed hysteretic models that capture the basic modes of cyclic deterioration in steel
49 components, namely strength, post-peak strength and unloading stiffness deterioration. Others
50 (Lignos and Krawinkler 2011; Lignos et al. 2019) have proposed ad hoc modifications to the Ibarra

51 et al. model's hysteretic rules in an effort to properly describe the hysteretic behavior of steel
52 members.

53 Point hinge models have become the main workhorse in collapse-risk assessment studies (FEMA
54 2009; NIST 2010), however, they exhibit considerable limitations. First, their calibration requires
55 large component datasets (Lignos and Krawinkler 2013) that may not be always available. Second,
56 point hinge models do not capture coupled geometric instabilities, and the effects of residual
57 stresses on steel structures (Mathur et al. 2012). Third, the above approaches do not consider
58 varying axial loads and bi-directional loading effects, nor do they capture axial shortening that
59 may be influential in estimating earthquake induced losses (Elkady et al. 2020). These are major
60 drawbacks, considering the findings from recent full-scale experimental studies (Suzuki and Lignos
61 2015; Ozkula et al. 2017; Elkady and Lignos 2018a; Cravero et al. 2020), along with corroborating
62 CFE analyses (Elkady and Lignos 2015a; Fogarty and El-Tawil 2015; Elkady and Lignos 2018b;
63 Wu et al. 2018).

64 The capability of standard flexibility- (Spacone et al. 1996) and displacement-based (Mari
65 1984) fiber-based beam-column elements to simulate the inelastic behavior of steel and composite-
66 steel structures is well established (Hajjar et al. 1998; Sivaselvan and Reinhorn 2002). Numerical
67 accuracy, for a viable computational expense, can be achieved by properly selecting the number
68 of fibers to discretize the cross-section (Kostic and Filippou 2012). Standard fiber beam-column
69 elements employ the plane-sections-remain-plane assumption that is violated by torsion warping
70 present in wide-flange steel profiles. Theoretical developments have been proposed to address this
71 challenge for fiber-based beam-column elements (Le Corvec 2012; Di Re et al. 2018). Inclusion of
72 the warping component is critical for evaluating wide-flange steel components subjected to torsion
73 and those that are susceptible to lateral-torsional buckling.

74 Continuum finite element component models are currently the only viable way to provide in-
75 sights into complex instability interactions prior to global and partial structural collapse (Miyamura
76 et al. 2015; Stoakes and Fahnestock 2016; Wu et al. 2018). CFE models are also suitable for detailed
77 studies of critical regions of metal structures (Kalochoiretis and Gantes 2011; Elkady and Lignos

78 2015a; Elkady and Lignos 2018b; Fogarty and El-Tawil 2015; Araújo et al. 2017). Furthermore,
79 it is acknowledged that CFE simulations can serve as benchmarks for theoretical developments of
80 advanced fiber beam-column elements, and for the further development of advanced experimental
81 techniques (Whyte et al. 2016).

82 A current difficulty in employing CFE models in structural analysis is that they are computation-
83 ally expensive for multiple nonlinear dynamic analyses of structures. Reducing the computational
84 expense of simulation models in aforementioned studies (Miyamura et al. 2015; Wu et al. 2018)
85 would be beneficial to increase the number of structural configurations and ground motions that
86 can be investigated within any time-frame. Such a consideration is particularly important in, e.g.,
87 incremental dynamic analysis (Vamvatsikos and Cornell 2002), in which the computational com-
88 plexity is further increased through the number of intensity levels analyzed for each ground motion.
89 There is a clear need to reduce the computational demands from CFE component models while
90 retaining the solution fidelity of this modeling approach. To achieve this goal, methods to reduce
91 the associated computational cost in CFE simulations should be further developed.

92 The approach advocated in this paper is to employ a mixed-dimension component macro model,
93 that combines domains of 1D beam-column elements with continuum domains comprised of 2D
94 shell or 3D solid elements. Here, the dimensionality of the element refers to the number of
95 dimensions used to parametrize the element geometry: 1D elements are lines, 2D elements are
96 surfaces, and 3D elements are volumes. The mixed-dimension macro model idea is illustrated
97 in Fig. 1a that shows the beam-column (Ω_1) and continuum (Ω_2) element domains for a wide-
98 flange cross-section. Macro models can capture material plasticity and local instabilities in the
99 continuum domains, while maintaining the computational efficiency of beam-column elements. A
100 chief issue in mixed-dimension macro models, and the focus of this paper, is that there is a need to
101 select an accurate coupling method between the beam-column and continuum domains that is also
102 computationally friendly.

Review of Coupling Methods

Coupling between the beam-column and continuum domains is typically accomplished through one of two means: the transition element approach, or the multipoint constraint (MPC) approach. One-dimension-to-continuum transition elements have been developed by Wagner and Gruttmann (2002), and were later extended by Chavan and Wriggers (2004) to include warping, and Koczubiej and Cichoń (2014) further extended these elements to the total Lagrangian formulation. More recently, Sadeghian et al. (2018) developed transition elements between 1D beam-column elements and 2D membrane elements for the analysis of reinforced concrete members. One limitation of transition elements is that they are typically less efficient than MPC approaches due to the proliferation of elements that connect all the nodes across both domains at the interface. Further limitations of transition elements include a proclivity to locking, and the need to treat such effects (Ho et al. 2010).

The MPC coupling approach specifies constraint equations among the relevant degrees of freedom (DOFs) between the two domains on the beam-column/continuum interface. The MPCs that form the coupling between domains can be implemented through any common constraint method (e.g., elimination, Lagrange multipliers, and the penalty method). Mixed-dimension MPC coupling methods have been developed by Monaghan et al. (1998) for coupling beam-column and solid domains by balancing the work done on the interface of each region. McCune et al. (2000, Shim et al. (2002) expanded on Monaghan et al. (1998)'s formulations to generalize for 1, 2, and 3D coupling. The notable limitations of this method are that linear constraint equations are enforced (i.e., the dependent DOFs have a linear relation to the independent DOFs), and that deformations due to warping are not transferred between the beam-column and continuum domains. Ho et al. (2010) proposed a multi-dimensional coupling for use with explicit time integration methods. Warping and shear deformations are not included in this method, and the reliance on explicit time integration limits the applicability of this approach. Song (2010) developed coupling between Timoshenko beam-column elements and 3D solid elements using transformation matrices. Again, warping was not included, and only linear material behavior and small deformations are considered. The lack

130 of warping transfer between the two domains limits the applicability of any coupling method for
131 components experiencing to nonuniform torsion or susceptible to lateral-torsional buckling.

132 Kinematic coupling constitutes another class of MPC methods. In this method, displacement
133 and/or rotation continuity of a dependent region of continuum element nodes is enforced based
134 on the displacements and rotations of an independent beam-column node. Existing formulations
135 (Dassault Systèmes 2014; Liu 2016) fall under the category of kinematic coupling as they enforce
136 displacement continuity in static problems, and a mixture of velocity and displacement continuity
137 in dynamic problems. Liu (2016) showed the capability of kinematic coupling utilizing nonlinear
138 constraint equations for solving problems involving finite-rotations. However, torsion warping is
139 again absent in these formulations. Incorporating warping into kinematic coupling, and studying
140 the effect of doing so, are two aims of this paper.

141 **Paper Objectives**

142 Component models that mix elements of varying fidelity have been used previously in the
143 assessment of steel structures (see e.g., Tada et al. (2008), Krishnan (2010), Sreenath et al. (2011),
144 Imanpour et al. (2016)), however, such studies have not focused on the effect of the coupling method
145 between the different domains. Further investigation into this matter is necessary to develop accurate
146 and efficient modeling recommendations for a wide range of steel beam-column components. The
147 main issues apparent in the reviewed coupling methods are that transition elements that include
148 warping may not be computationally efficient when compared with the MPC approach, and that
149 existing MPC approaches do not consider warping that can be critical for beam-columns susceptible
150 to coupled local and lateral-torsional buckling. Furthermore, nonlinear constraint equations should
151 be should be employed for modeling collapse limit states often of interest in earthquake engineering.

152 An MPC kinematic coupling method that includes torsion warping is proposed to address the
153 aforementioned considerations. This paper focuses on answering the following questions: What
154 is the effect of warping-inclusive coupling on simulation results? When are formulations with
155 linear constraint equations acceptable? What are the computational benefits of the component
156 macro model approach? Linear and nonlinear versions of the proposed coupling method are

157 implemented; the proposed coupling method is found to be easily compatible with existing finite
 158 element analysis software typically used in practice. A series of computational case studies are
 159 then used to evaluate each of questions posed above using the proposed MPC formulation and an
 160 existing coupling method that is available in commercial software.

161 PROPOSED COUPLING METHOD

162 Beam-Column Element Kinematics

163 A coupling strategy for beam-column and continuum elements requires an understanding of
 164 the governing element kinematics. The beam-column kinematics used herein are based on a line
 165 of centroids and a set of cross-section planes that rotate about each of the centroid points, see
 166 e.g., [Simo and Vu-Quoc \(1991\)](#). Following this reference, a warping function is also defined on
 167 the cross-section to incorporate out-of-plane torsion warping. Each beam-column element node is
 168 assumed to have three displacement DOFs, three rotation DOFs, and one torsion warping DOF.

169 Beam kinematics are defined by material points, denoted \mathbf{x}_{mp}^b , where the subscript indicates
 170 that this is a material point and the superscript indicates the beam-column element. The position
 171 of any material point in the cross-section defined by the beam element formulation is as follows:

$$172 \quad \mathbf{x}_{mp}^b(\xi, \eta, \zeta) = \mathbf{x}(\zeta) + \xi \mathbf{n}_1(\zeta) + \eta \mathbf{n}_2(\zeta) + w(\zeta) \psi(\xi, \eta) \mathbf{t}(\zeta), \quad (1)$$

173 where ζ is the coordinate along the element centerline, ξ and η are the distances measured along
 174 the \mathbf{n}_1 , \mathbf{n}_2 axes in the undeformed configuration, $\mathbf{x}(\zeta)$ is the position of the centroid along the
 175 centerline in the undeformed configuration, $w(\zeta)$ is the warping amplitude, $\psi(\xi, \eta)$ is the warping
 176 function, and $\mathbf{t}(\zeta)$ is the axis in the direction of the cross-section normal. The representation of
 177 these parameters is shown in Fig. 2a for a wide-flange profile, and leads to the limits of $0 \leq \zeta \leq L$,
 178 $-b_f/2 \leq \xi \leq b_f/2$ and $-d/2 \leq \eta \leq d/2$, where L is the member length; b_f is the flange width;
 179 and d is the full cross-section depth. The first term in Eqn. 1 is the position of the cross-section
 180 with respect to the centerline, the second and third terms represent the cross-section plane spanned
 181 by \mathbf{n}_1 and \mathbf{n}_2 , and the fourth term is the out-of-plane deformation due to torsion warping.

182 Only wide-flange sections are considered within the scope of this paper, however, the proposed
 183 coupling method may be used with other cross-sections provided that the warping function is readily
 184 available at each point on the cross-section. The warping function used in this paper is based on
 185 elastic homogeneous thin-walled open cross-sections, and for wide-flange cross-sections can be
 186 simply defined as (Chen and Atsuta 2008)

$$187 \quad \psi(\xi, \eta) = \xi \eta. \quad (2)$$

188 **Nonlinear Definition of the Constraint Equations**

189 The kinematic coupling method proposed in this paper is composed of constraint equations that
 190 relate the beam-column and continuum domains, as defined in Fig. 2b. The beam-column domain
 191 is Ω_1 , the continuum domain is Ω_2 , and the interface between these two domains is Γ . The proposed
 192 coupling method stipulates that the beam-column node is coupled to the three displacement DOFs
 193 of the continuum nodes on the interface, therefore, coupling of rotation DOFs in the continuum
 194 domain are neglected (e.g., in shell elements). This method is referred to as the Warping-Inclusive
 195 Kinematic Coupling, or WIKC, herein, and can be identified as an enhancement to kinematic
 196 coupling methods, for instance, in Abaqus (Dassault Systèmes 2014). Each of the constraint
 197 equations are a function of seven variables owing to the seven DOFs of the beam-column node, and
 198 in total $3N$ equations are defined for N continuum nodes.

199 First, the constraints for a single continuum node are presented without warping, and afterwards
 200 the warping term is included. The nonlinear, rigid-body coupling constraint equations without
 201 warping are written succinctly in matrix-vector form for a single node as

$$202 \quad \mathbf{u}^c = \mathbf{u}^b + \mathbf{R}^b \mathbf{l} - \mathbf{l}, \quad (3)$$

203 where \mathbf{u}^c is the vector of continuum displacements, \mathbf{u}^b is the vector of beam-column node dis-
 204 placements, \mathbf{l} is the link vector that relates the continuum node initial position to the beam-column
 205 node initial position, ($\mathbf{l} = \mathbf{x}^c - \mathbf{x}^b$, \mathbf{x}^c is the initial position of the continuum element node, and

206 \mathbf{x}^b is the initial position of the beam-column node, as shown in Fig. 2a). The term $\mathbf{R}^b \mathbf{l}$ is the link
 207 rotated into the deformed configuration by the rotation matrix \mathbf{R}^b . The definition of each of these
 208 variables is shown in Fig. 2b, and the deformed configuration is shown in Fig. 2c.

209 The rotation matrix, \mathbf{R}^b , is formed from the rotation vector of the beam-column node, $\boldsymbol{\phi}^b$, using
 210 the well-known Rodrigues formula (Rodrigues 1840):

$$211 \quad r = \|\boldsymbol{\phi}^b\|, \quad \mathbf{r} = \boldsymbol{\phi}^b / r, \quad (4a)$$

$$212 \quad \mathbf{R}^b = \cos[r] \mathbf{I} + (1 - \cos[r]) \mathbf{r} \mathbf{r}^T + \sin[r] [\mathbf{r}]_{\times}, \quad (4b)$$

214 where \mathbf{I} is the 3×3 identity matrix, and $[\mathbf{r}]_{\times}$ is the skew-symmetric matrix formed from \mathbf{r} , i.e.,

$$215 \quad [\mathbf{r}]_{\times} = \begin{bmatrix} 0 & -r_3 & r_2 \\ r_3 & 0 & -r_1 \\ -r_2 & r_1 & 0 \end{bmatrix}. \quad (5)$$

216 Including warping, the constraint equations that constitute the warping-inclusive kinematic
 217 coupling method become

$$218 \quad \mathbf{u}^c = \mathbf{u}^b + \mathbf{R}^b \mathbf{l} - \mathbf{l} + \psi w^b \mathbf{R}^b \mathbf{t}, \quad (6)$$

219 where ψ is the warping function evaluated at ξ and η of the node, w^b is the value of the warping DOF
 220 at the beam-column node, and the term $\mathbf{R}^b \mathbf{t}$ is the orientation of the local \mathbf{t} -axis in the deformed
 221 configuration. Finally, the standard, or homogenous, form of the constraint equations is

$$222 \quad \mathbf{f} := \mathbf{u}^c - \mathbf{u}^b - \mathbf{R}^b \mathbf{l} + \mathbf{l} - \psi w^b \mathbf{R}^b \mathbf{t} = 0. \quad (7)$$

223 Linearized Constraint Equations

224 Linearized constraint equations are necessary for implementation of the coupling in a nonlinear
 225 incremental-iterative analysis (e.g., Newton-Raphson). The key components of the linearized
 226 constraint equations are the constraint coefficient matrices, \mathbf{A}_1 and \mathbf{A}_2 , that are based on the

227 standard form of the constraint equations. These two matrices are the coefficients of the beam-
 228 column and continuum nodes, respectively, from the linearized constraint equation. Linearizing
 229 Eqn. 7, A_1 and A_2 are defined in Eqn. 8 as follows:

$$230 \quad \delta \mathbf{f} = \mathbf{A}_1 \delta \mathbf{u}^c + \mathbf{A}_2 \begin{bmatrix} \delta \mathbf{u}^b \\ \delta \boldsymbol{\theta}^b \\ \delta \mathbf{w}^b \end{bmatrix} = 0, \quad (8)$$

231 where $\delta \boldsymbol{\theta}^b$ is the linearized rotation vector. Carrying out the linearization, the following expression
 232 is obtained:

$$233 \quad \delta \mathbf{f} = \delta \mathbf{u}^c - \delta \mathbf{u}^b - \mathbf{R}^b \mathbf{l} \times \delta \boldsymbol{\theta} - \psi \mathbf{w}^b \mathbf{R}^b \mathbf{t} \times \delta \boldsymbol{\theta} - \psi \mathbf{R}^b \mathbf{t} \delta \mathbf{w}^b, \quad (9)$$

234 where, for any rotation field, $\delta(\mathbf{R}^b \mathbf{l}) = \delta \boldsymbol{\theta} \times \mathbf{R}^b \mathbf{l}$ (see, e.g., Sec. 1.3.1 of [Dassault Systèmes \(2014\)](#)).
 235 Additionally in Eqn. 9, the term $\delta \mathbf{l} = 0$ because this vector is considered to be constant throughout
 236 the analysis (i.e., deformation of the cross-section due to Poisson's effect is neglected). From
 237 Eqn. 9, the A_1 matrix related to the displacement s of the beam-column node is equal to the identity
 238 matrix, \mathbf{I} , since all the coefficients are equal to unity. Collecting the remaining terms in Eqn. 9,
 239 and using the matrix definition of the cross-product, the A_2 matrix of dimension 3×7 becomes

$$240 \quad \mathbf{A}_2 = \left[\mathbf{A}_2^{disp}, \mathbf{A}_2^{rot}, \mathbf{A}_2^{warp} \right] = \left[-\mathbf{I}, -[\mathbf{R}^b \mathbf{l} + \psi \mathbf{w}^b \mathbf{R}^b \mathbf{t}^b]_{\times}, -\psi \mathbf{R}^b \mathbf{t} \right]. \quad (10)$$

241 To close, a few remarks are made regarding A_2 :

- 242 • The $[\mathbf{R}^b \mathbf{l}]_{\times}$ term can be interpreted as forces acting at the continuum node due to bend-
 243 ing/(pure)torsion acting on the beam-column node in the current deformed configuration.
- 244 • The $[\psi \mathbf{w}^b \mathbf{R}^b \mathbf{t}]_{\times}$ term can be interpreted as a nonlinear effect of warping that arises because
 245 of the displacement component in the local \mathbf{t} -axis between the continuum and beam-column
 246 nodes.
- 247 • The coupling method is nonlinear because the A_2^{rot} and A_2^{warp} matrices depend on the

248 current rotation \mathbf{R}^b , therefore, the \mathbf{A}_2 matrix needs to be re-computed at each iteration in
 249 the analysis.

250 *Linear Coupling Method*

251 A linear version of the WIKC method is derived for use in evaluating linear coupling methods.
 252 The linear constraint coefficient matrix, \mathbf{A}^{lin} , can be recovered from Eqn. 10 by considering
 253 the current configuration always equal to the initial configuration. This is done by replacing
 254 $-\left[\mathbf{R}^b \mathbf{l} + \psi \mathbf{w}^b \mathbf{R}^b \mathbf{t}\right]_{\times}$ with $-\left[\mathbf{l}\right]_{\times}$ in \mathbf{A}^{rot} , and replacing $-\psi \mathbf{R}^b \mathbf{t}$ with $-\psi \mathbf{t}$ in \mathbf{A}^{warp} . With these
 255 considerations, the linear version of the \mathbf{A}_2 matrix becomes

$$256 \quad \mathbf{A}_2^{lin} = \left[-\mathbf{I}, -\left[\mathbf{l}\right]_{\times}, -\psi \mathbf{t} \right]. \quad (11)$$

257 The governing linear constraint equations can be recovered by applying \mathbf{A}_2 to the vector of beam-
 258 column DOFs, and considering that $l_3 = 0$ as the continuum and beam-column nodes are assumed
 259 to be in the same plane initially:

$$260 \quad \mathbf{u}_c = \mathbf{A}_2^{lin} \begin{bmatrix} \mathbf{u}^b \\ \boldsymbol{\phi}^b \\ \mathbf{w}^b \end{bmatrix} \Rightarrow \mathbf{u}_c = \begin{bmatrix} u_1^b - \phi_3^b \eta, \\ u_2^b + \phi_3^b \xi, \\ u_3^b + \phi_1^b \eta - \phi_2^b \xi + \xi \eta \mathbf{w}^b \end{bmatrix}. \quad (12)$$

261 **CASE STUDIES**

262 A series of case studies are investigated in this paper to: (a) validate the proposed WIKC method,
 263 illustrate the importance of including warping in the constraint equations, (b) assess the applicability
 264 of the linear coupling method, (c) and highlight the computational efficiency of the proposed macro
 265 models. To achieve these objectives, four computational models are compared for each of the cases
 266 described in subsequent sections: (1) a full-shell model that represents the continuum “benchmark”
 267 analysis (denoted as Full-shell); (2) a beam-shell macro model using a “built-in” kinematic coupling
 268 formulation that does not transfer warping across the interface (denoted as Macro Built-in); (3) a
 269 beam-shell macro model using the proposed nonlinear WIKC (denoted as Macro Warping); and

270 (4) a beam-shell macro model using the proposed linear WIKC (denoted as Macro Lin. Warping).
271 All of the computational work in this paper is carried out using Abaqus v6.14 (Dassault Systèmes
272 2014). Both the linear and nonlinear versions of the WIKC method are implemented in Abaqus
273 using MPC user subroutines; the source code, instructions for use, and examples are available in
274 Hartloper (2020). The following sections provide a description of the case studies, their links with
275 practical applications, and a set of general modeling recommendations. Afterwards, the results for
276 each case are presented and discussed.

277 Case Studies Overview

278 The case studies investigated in this paper are summarized in Table 1. This table gives a
279 brief description of the primary mode of deformation, the components and their respective cross-
280 sections, and the stability of the anticipated equilibrium path. The objectives of Case Study 1 are
281 to demonstrate the error in the elastic torsional stiffness of mixed-dimension macro models when
282 warping is not included in the coupling formulation, and to identify the limits of the proposed macro
283 model approach when twisting is significant. Case Studies 2–4 demonstrate the implications of this
284 issue in the context of steel components subjected to cyclic loading. These examples are based on
285 structural components in steel moment-resisting frames (MRFs), subjected to both quasi-static and
286 dynamic loading, as shown schematically in Fig. 3. Through these four case studies, the proposed
287 macro model approach and coupling method are evaluated for main structural components in steel
288 MRFs.

289 *Case Study 1: Nonuniform Torsion*

290 Case Study 1 is based on a seminal experiment conducted by Farwell and Galambos (1969)
291 using a 6×6 -25 beam of ASTM-A36 (nominal $f_y = 250$ MPa) steel subjected to a central torque.
292 The geometric properties of the 6×6 -25 beam are provided in Table 2, and a schematic of the
293 test set-up is provided in Fig. 4. The test consists of a steel beam fixed against rotation at the ends
294 but free to warp. A torque is applied at the center of the beam through the circular loading plate.
295 The beam ends are assumed to be restricted in axial displacement due to friction at the beam end
296 supports, as this condition provides the best match with the test data.. For this reason the centroid

297 of the beam is considered as axially fixed at the ends. The equilibrium path in Case Study 1 is
298 stable (i.e., no buckling occurs) as the beam is only subjected to torsion. The continuum lengths
299 are nominally chosen as $L_{\Omega_2} = 0.25L = 482.5$ mm at both member ends for the macro models.

300 *Case Study 2: Interior Subassembly*

301 Case Study 2 focuses on an interior subassembly, in this case represented by the DBBW specimen
302 tested by Engelhardt et al. (2000) as a part of the SAC¹ Program (FEMA 2000). The beams in
303 the subassembly have a W36X150 cross-section, and the column is a W14X398, dimensions of
304 the components are provided in Table 2, and a schematic of the subassembly is shown in Fig. 5b.
305 This table also includes the normalized LTB slenderness per CEN (2005), the ratio of unbraced
306 length to weak-axis radius of gyration (L_b/r_y), and the limiting length for inelastic LTB (L_r) per
307 ANSI/AISC 360-16 (AISC 2016). The material for all components is ASTM A572 Gr. 50 steel
308 ($f_y = 345$ MPa). The beams have roller supports near the ends and lateral supports at the ends,
309 and a cyclic displacement-controlled load is applied at the column top. The column bottom is
310 pinned, and the top is fixed against out-of-plane displacements and has a flexible torsional support
311 that is modeled with a stiffness equivalent to two 1.5 m W14X150 beams. Both beam-to-column
312 connections include radius-cut reduced beam sections (RBS), and the subassembly was designed
313 with a balanced panel zone concept that leads to yielding in the panel zone and buckling in the
314 RBS region, therefore, the equilibrium path is designated as unstable. Based on observations of
315 the Full-shell model, the continuum lengths are chosen to be approximately 400 mm greater than
316 the extend of the RBS cut-out in the beams ($L_{\Omega_2} = 1300$ mm), and approximately 400 mm greater
317 than the beams on both sides for the column ($L_{\Omega_2} = 1700$ mm).

318 *Case Study 3: Quasi-Static Collapse-Consistent Loading of First-story Column*

319 Case Study 3 focuses on a typical first-story column with a relatively compact cross-section
320 ($b_f/2t_f = 5.92$, $h/t_w = 33.2$), in this case represented by the C5 test carried out by Elkady and
321 Lignos (2018a). The column cross-section is a W24X146, with a length of 3.9 m, the geometric

¹Joint venture between the Structural Engineers Association of California (SEAOC), the Applied Technology Council (ATC), and California Universities for Research in Earthquake Engineering (CUREe)

properties are summarized in Table 2. The column is not critical for LTB since $\bar{\lambda}_{LT} < 0.4$. A unidirectional collapse consistent load protocol (Suzuki and Lignos 2020) is applied in the strong axis of the column (u_y), and a constant compressive 20 % of the measured axial yield load is applied at the column top ($-F_z$), as illustrated in Fig. 5c. Rotations and displacements are fixed at the column base, and a rotationally flexible boundary in the strong axis is assumed at the column top by synchronizing ϕ_x with u_y . The basis of the flexible boundary is to obtain an inflection point at $z = 3/4L$ when the column is elastic, representative of first-story columns in steel moment-resisting frames Elkady and Lignos (2018a). The equilibrium path is classified as unstable because local buckling is observed in the test, thereby causing cyclic deterioration in strength and stiffness. The continuum lengths are chosen as $L_{\Omega_2} = 0.5L = 900$ mm at both member ends for the macro models to capture the local buckling at the member ends.

Case Study 4: Column Nonlinear Response History Analysis

Case Study 4 focuses on an equivalent single-degree-of-freedom type representation of a typical first story column. The column selected for this example is based on the interior first-story column in a prototype four-story steel MRF designed for urban California (Elkady and Lignos 2015b). The column cross-section is a W24X94 with a length of 5500 mm, the geometric properties are summarized in Table 2, and a schematic of the model is provided in Fig. 5d. The criticality of including warping in the coupling formulation is demonstrated in this case since the column has a typical cross-section and is susceptible to inelastic lateral-torsional buckling ($\bar{\lambda}_{LT} > 0.4$).

All displacements and rotations are fixed at the column bottom, and out-of-plane displacements and all rotations are fixed at the column top. A constant axial load corresponding to 20 % of the expected axial yield strength of the cross-section ($F_z = 1300$ kN) is applied at the top of the column, and the Northridge 1994 Canoga Park record is applied to the base of the column ($a_{g,y}$). The first-mode period of the target prototype structure is about 1.5 s (Elkady 2016), therefore, the mass of the column is chosen such that the first-mode period is equal to 1.5 s. This procedure results in a mass of 766.5 s²N/mm, and 2 % mass proportional damping is assumed. A frequency analysis is conducted to validate the computed mass and the results are presented later. The shell lengths

349 are chosen as $L_{\Omega_2} = 0.3L = 1650$ mm at both member ends for the macro models to capture the
350 coupled buckling along the member length.

351 **Nonlinear Finite Element Modeling Approach**

352 Modeling guidelines for the Full-shell models are based on those of [Elkady and Lignos \(2018b\)](#),
353 and the macro models are then adapted from the full-shell models. A later section also includes
354 a methodology for generating and imposing imperfections for continuum mechanics problems
355 containing an unstable equilibrium path, and afterwards a summary of the model and imperfection
356 properties is provided for all the case studies.

357 Numerical details of the analyses carried out in Abaqus v6.14 are outlined for clarity. Implicit
358 time integration is used for both the quasi-static and dynamic problems. The system of equilibrium
359 equations is solved using Newton's method with double precision. The default convergence criteria
360 of 0.5 % on the relative force and moment residuals is used for all analyses.

361 Based on [Elkady and Lignos \(2018b\)](#), four-node reduced integration shell elements (S4R) are
362 used in the continuum domains. The Abaqus enhanced hourglass stiffness control is used ([Dassault
363 Systèmes 2014](#)), and five Simpson integration points are used throughout the shell thickness. A
364 mesh size of <25 mm is used in the continuum domains where buckling may occur, and the element
365 size is relaxed in the column of Case Study 2 since only yielding of the panel zone occurs. Linear,
366 two-node beam-column elements with torsion warping (B31OS) are used in the beam-column
367 element domains. These are displacement-based beam-column elements with a single integration
368 point at the center of the element, and 7-DOFs at each node. Cross-section properties and forces
369 are evaluated in these beam-column elements at five integration points in each flange, and five
370 integration points along the web ([Dassault Systèmes 2014](#)). A minimum of four beam-column
371 elements are used in each Ω_1 domain so that possible member buckling can be captured in the
372 macro model. Extents of the beam-column and shell element domains, i.e., the length L_{Ω_2} in
373 Fig. 1a, are provided for all the cases in Table 3.

374 The Voce-Chaboche (VC) nonlinear kinematic/isotropic hardening material model native to
375 Abaqus v6.14 is used in all the beam-column and shell domains to represent the ASTM A992 Gr. 50

376 and ASTM A572 Gr. 50 materials subjected to cyclic straining. Consistent model parameters for
377 the A992 Gr. 50 steel are taken from [de Castro e Sousa et al. \(2020b\)](#). VC model parameters for
378 the A572 Gr. 50 steel are calibrated using the tensile-only approach of [de Castro e Sousa et al.](#)
379 [\(2020a\)](#) using the SAC average stress-strain curve ([Engelhardt et al. 2000](#)). Employed parameters
380 for both materials are provided in Table 4, where a Poisson's Ratio of $\nu = 0.3$ is always assumed.
381 One limitation of the employed Abaqus v6.14 beam-column elements is that only one material may
382 be specified for the element. The flange material properties are assumed throughout the beam-
383 column domains because yielding is primarily expected to occur in the flanges due to the axial
384 stress gradient from bending. Residual stresses are not considered in any of the numerical models
385 because the beam-column elements in Abaqus v6.14 do not allow for residual stress variations
386 through the cross-section, this issue is discussed later in the Limitations section.

387 *Modeling Exceptions for Case Study 1*

388 The following exceptions to the aforementioned guidelines are made for Case Study 1: the mesh
389 size is slightly smaller than that recommended by [Elkady and Lignos \(2018b\)](#) due to the smaller
390 cross-section dimensions, and an increased number of quadratic beam-column elements (B32OS)
391 are used in Ω_1 . The increased elements and additional integration point along the length are required
392 to capture the yielding throughout the member, whereas this is not necessary for the other case
393 studies since yielding is focused at the member ends in the continuum domains. Furthermore, a
394 beam-column element only model (denoted "Full-beam") is used in this case study to compare a
395 beam-column element only model with a shell element only model. An exception is also made for
396 the ASTM-A36 material properties in this case study: a piece-wise isotropic hardening model is
397 used to represent this steel material since only monotonic loading is applied. The parameters for
398 the ASTM-A36 material are $E = 213400$ MPa, $\nu = 0.3$, $\sigma_{y,0} = 285$ MPa and hardening defined by
399 289 MPa at $\varepsilon^p = 0.01329$ and 876.2 MPa at $\varepsilon^p = 0.094$ as assumed in [Pi and Trahair \(1995\)](#).

400 **Imperfection Methodology**

401 Imperfections are critical when geometric instabilities are expected in nonlinear analysis prob-
402 lems ([Galambos 1998](#); [Ziemian 2010](#); [AISC 2016](#)), for this reason, care is taken in describing the

403 approach used to apply imperfections. Member out-of-straightness and out-of-plumbness imper-
404 fections are deemed critical for flexural buckling modes, and local flange and web imperfections are
405 deemed critical for local buckling modes. Twisting imperfections are also considered to be critical
406 for modes associated with lateral-torsional buckling. Flexural buckling modes are not critical in the
407 analyses examined herein, and therefore, out-of-straightness and out-of-plumbness imperfections
408 are not considered.

409 Typically, imperfections may be included by applying scaled buckling modes from elastic
410 eigenvalue analysis to the geometrically perfect model (Fogarty and El-Tawil 2015; Elkady and
411 Lignos 2018b; Cravero et al. 2020). One issue with this typical method is that the similitude
412 between the full-continuum and macro models is not guaranteed because the presence of the
413 beam-continuum interface will influence the computed buckling modes. Using the exact same
414 imperfections in the full-shell and macro models is considered important to remove a potential
415 source of bias when comparing the two modeling approaches. An alternative method is proposed
416 in this study to derive local imperfection geometries that are applied directly to the shell domains.
417 This proposed method also addresses an anticipated challenge of applying geometric imperfections
418 to members in system-level simulation studies where the member buckling modes may not be
419 available for each individual component.

420 The proposed imperfection method, implemented in the Python package `pywikc` (Hartloper
421 2020), defines a local imperfection geometry according to elastic plate buckling theory. The
422 shape of the imperfection is defined as a function of the buckling wavelength, L_{bw} , and the
423 maximum imperfection amplitude. The buckling wavelength is determined using elastic eigenvalue
424 buckling analysis of the component, and the maximum imperfection amplitude is based on previous
425 studies and measurements of wide-flange cross-sections (Hartloper and Lignos 2019). First, the
426 imperfection shapes are defined, then methods for obtaining the maximum amplitudes and L_{bw} are
427 defined.

428 Equations describing the buckled shape along the width of the flanges and web are adapted
429 from Hill (1940) and Haaijer (1956). The mathematical model for the half-flange plate is shown in

430 Fig. 6. A uniform compressive stress, σ , is assumed to act along the two fixed edges, while one
 431 edge is free and the other edge has a rotational restraint (RR) from the web. The shape along the
 432 flange width in the \mathbf{n}_1 direction is described by

$$433 \quad v_{\xi}(\tilde{\xi}) = \tilde{\xi} + \frac{\epsilon}{2a_3} \left(\tilde{\xi}^3 + a_1 \tilde{\xi}^4 + a_2 \tilde{\xi}^3 + a_3 \tilde{\xi}^2 \right), \quad (13)$$

434 where $a_1 = -4.963$, $a_2 = 9.852$, $a_3 = -9.778$, ϵ is the relative restraint per unit width provided by
 435 the web, and $\tilde{\xi} = \xi/(b_f/2)$. The model for the web plate is similar to that of the flange, but both
 436 unloaded edges have a rotational restraint due to the flanges. The shape along the width of the web
 437 in the \mathbf{n}_2 direction is

$$438 \quad v_{\eta}(\tilde{\eta}) = \frac{\pi\epsilon}{2} \left(\tilde{\eta}^2 - 0.25 \right) + (1 + \epsilon/2) \cos(\pi\tilde{\eta}), \quad (14)$$

439 where ϵ is the relative restraint per unit width provided by the flanges, and $\tilde{\eta} = \eta/(d - t_f)$. The
 440 shape of both the flange and web plates in the t direction is needed to complete the imperfection. A
 441 function is defined to represent a single buckling wave that satisfies the fixed boundary conditions
 442 at the loaded edges, a suitable function is

$$443 \quad v_{\zeta}(\zeta) = \sin^2[\pi \zeta / L_{bw}]. \quad (15)$$

444 The final buckled shape is obtained by multiplying v_{ξ} with v_{ζ} for the flange, and v_{η} with v_{ζ}
 445 for the web. The complete buckled shape for the flange is shown in Fig. 6b. Contours of the two
 446 functions v_{ξ} and v_{ζ} are shown projected onto the axes to give a sense of the effect of these functions
 447 on the imperfection geometry. The normalized vector of the flange imperfection is obtained from
 448 Eqns. 13 and 15:

$$449 \quad \mathbf{v}_f(\tilde{\xi}, \zeta) = \frac{v_{\xi}(\tilde{\xi})v_{\zeta}(\zeta)}{\max[v_{\xi}(\tilde{\xi})v_{\zeta}(\zeta)]} \mathbf{n}_2. \quad (16)$$

450 The normalized vector of the web imperfection is obtained from Eqns. 14 and 15:

$$451 \quad \mathbf{v}_w(\tilde{\eta}, \zeta) = \frac{v_{\eta}(\tilde{\eta})v_{\zeta}(\zeta)}{\max[v_{\eta}(\tilde{\eta})v_{\zeta}(\zeta)]} \mathbf{n}_1. \quad (17)$$

452 The max is used in these equations so that the maximum imperfection amplitude can easily be
 453 made equal to a pre-specified value.

454 Finally, local imperfection fields for the entire member are defined through \mathbf{v}_{flange} and \mathbf{v}_{web} :

$$455 \quad \mathbf{v}_{flange} = \begin{cases} a_f \mathbf{v}_f(\tilde{\xi}, \zeta) & \text{if } 0 \leq \zeta \leq L_{bw} \\ -a_f \mathbf{v}_f(\tilde{\xi}, \zeta - (L - L_{bw})) & \text{if } L - L_{bw} \leq \zeta \leq L \end{cases} \quad (18a)$$

$$456 \quad \mathbf{v}_{web} = \begin{cases} a_w \mathbf{v}_w(\tilde{\eta}, \zeta) & \text{if } 0 \leq \zeta \leq L_{bw} \\ -a_w \mathbf{v}_w(\tilde{\eta}, \zeta - (L - L_{bw})) & \text{if } L - L_{bw} \leq \zeta \leq L \end{cases} \quad (18b)$$

457

458 where a_f is the maximum flange imperfection amplitude, and a_w is the maximum web imperfec-
 459 tion amplitude. The different cases in these equations lead to an anti-symmetric in-plane local
 460 imperfection pattern at the bottom and top of the member, i.e., the imperfection is “in-wards” at one
 461 end and “out-wards” at the other. This mode is chosen on the basis of recommendations validated
 462 with beam-column experiments (Suzuki and Lignos 2015; Elkady and Lignos 2018a; Cravero et al.
 463 2020), and also agrees with expected cross-section imperfections due to the hot-rolling process and
 464 manufacturing (e.g., welding) (CEN 1993; ASTM 2016). Fig. 7b illustrates the anti-symmetric
 465 buckling pattern applied to an analysis model, and Fig. 7c shows the local buckling pattern present
 466 at the base of a W24X84 column subjected to 20 % axial load and a symmetric cyclic lateral loading
 467 history.

468 The local buckling wavelength, L_{bw} , of the local imperfections is unknown through the afore-
 469 mentioned procedure, and is determined in this study by matching with elastic eigenvalue buckling
 470 analysis in Abaqus. The length L_{bw} is chosen as the wavelength of the end-most local buckle present
 471 in a local buckling dominated mode. This end-most wavelength is deemed to be critical because
 472 local buckling is known to initiate at the member ends due to the moment gradient in columns
 473 subjected to lateral loads (Elkady and Lignos 2018a). A local buckling dominated mode from
 474 eigenvalue analysis is shown in Fig. 7a with the proposed method for applying local imperfections
 475 in Fig. 7b.

476 The last ingredient of the local imperfections are the maximum amplitudes a_f and a_w . The
477 local imperfection amplitudes are based on the compatible minimum of $d/300$ and $b_f/250$ that
478 have been used in prior studies based on measured imperfections (Hartloper and Lignos 2019),
479 and are similar to those in Elkady and Lignos (2018b). Compatibility in this proposed method is
480 defined by maintaining the 90 degree angle between the flange and web plate centerlines, therefore,
481 only one of the maximum amplitudes a_f or a_w will be reached depending on the section geometry.
482 Note that these imperfection amplitudes are below the tolerances set forth in standards such as
483 (CEN 1993; ASTM 2016).

484 Local imperfections are incorporated into to the simulation models by applying the imperfection
485 fields, Equations 18a and 18b, to the continuum domains. This method generates a set of nodal
486 perturbations that can be easily applied to the initially perfect geometry. The computation of the
487 local imperfection geometries has been implemented by the authors in the Python package `pywikc`
488 for wide-flange cross-sections (Hartloper 2020).

489 Twisting imperfections, occurring due to base plate welding, have typically been applied simi-
490 larly to local imperfections by applying a scaled buckling mode, or the nodal perturbation could be
491 specified directly. In the context of beam-shell macro models, however, the twisting imperfection
492 cannot be applied as an initial geometric imperfection in Abaqus because only initial displacements
493 can be specified to the nodes. This is an issue because the twisting imperfection is specified about
494 the member centerline, and therefore, the beam-column element centerline only has a rotation, and
495 does not have a displacement.

496 Similitude between the full-shell and macro models is obtained in this case by applying a torque
497 at the center of the model that leads to a twist equivalent to those measured in full-scale experiments,
498 similar to the notional load concept (AISC 2016). Twist magnitudes measured in Elkady (2016)
499 are used as a basis of expected amplitudes. The average twist magnitude measured at the column
500 top was 0.6 %rad, the minimum was 0.0 %rad, and the maximum was 1.5 %rad. Torques are
501 applied that lead to a mid-height twist equal to half the top twist assuming that initial angle of
502 twist is constant along the member. Concentrated torques are simple to apply to the beam-column

503 elements by ensuring a node exists at the center of the beam-column domain, and a distributed
504 coupling in Abaqus v6.14 is used to apply the concentrated torque to the full-shell models in a
505 region around the mid-height of the member.

506 The imperfection parameters for all the components included in the case studies are provided
507 in Table 3. For the beams in Case Study 2, ν_{flange} and ν_{web} are applied to the entire RBS region
508 ($L_{bw} = 686$ mm) with an offset equal to the distance from the beam end to the start of the radius
509 cut. For Case Studies 3 and 4, the length of the local buckling wave was found to be around $1.2d$.
510 The twisting imperfection in Case Study 3 is based on the measured value, while the twisting
511 imperfection in Case Study 4 is chosen near the maximum of the measured values in [Elkady and](#)
512 [Lignos \(2018a\)](#). Finally, no imperfections are included in components with stable equilibrium
513 paths because geometric instabilities are not expected, thereby diminishing the importance of
514 imperfections ([Galambos 1998](#); [Gantes and Fragkopoulos 2010](#); [Ziemian 2010](#)).

515 **CASE STUDY RESULTS**

516 Results in the form of component behavior and computational effort are reported for each of
517 the case studies. Computational effort in each case is measured in three possible ways: the total
518 number of DOFs in the model, the amount of memory required to run the analysis, and the number
519 of iterations required throughout the analysis. The total number of DOFs is representative of the
520 size of the problem being solved, and is correlated to the effort required to solve each iteration
521 of the Newton-Raphson method. The memory required represents a base-line requirement to run
522 the numerical model. The number of iterations required is indicative of the rate of convergence;
523 the rate of convergence can be used to validate the implementation of the WIKC method, and is
524 a major factor in the total analysis time. Direct measurements of the analysis time are not given
525 herein because they are highly dependent on the computational system used to solve the problem,
526 whereas the included metrics are independent of the utilized system.

527 **Case Study 1: Nonuniform Torsion Results**

528 Torque-twist responses of the finite element models along with the physical data is shown
529 in Fig. 8. From Fig. 8a, it is clear that the Full-shell model captures the component behavior

530 throughout the entire load path, while the other modeling options may only be accurate in the initial
531 loading stages (see Fig. 8b). The Macro (Warping) model with nonlinear WIKC begins to lose
532 accuracy with respect to the Full-shell model after a twist of around 0.25 rad because the Abaqus
533 beam-column elements are only valid for small angles of twist (Dassault Systèmes 2014), as seen
534 in the Full-beam model response as well. Results in Fig. 8b also indicate that the linear WIKC
535 method is viable for components that experience twists of up-to around 0.05 rad. In the context
536 of steel MRF components, the maximum observed twist in full-scale experiments on wide-flange
537 columns is in the neighborhood of 0.10 rad (Elkady 2016; Elkady and Lignos 2018a), therefore,
538 the Macro (Warping) model employing the nonlinear WIKC at beam-continuum interfaces should
539 be suitable for most applications, while the linear version presents a limitation in this regard.

540 A notable divergence is found in the elastic torsional stiffness of the Macro (Built-in) model
541 compared with the other options, as the elastic torsional stiffness is computed to be 226 kN-
542 m/rad and this quantity is around 90 kN-m/rad for the Full-shell model. Differences in the elastic
543 stiffnesses is clearly visible in Fig. 8b. The built-in kinematic coupling in Abaqus, that does not
544 transfer warping, creates a warping-fixed boundary in the continuum domains at the interface, this
545 in-turn leads to the increase in the torsional stiffness. This issue will have later implications in the
546 response of steel MRF components subjected to cyclic loading.

547 Accuracy of the coupling method can also be assessed in this case by comparing the von Mises
548 equivalent stress distributions at the interface shell elements in Fig. 9 near the point of yielding
549 ($M_z = 11.25$ kN-m). The stress distribution of the Macro (Warping) model is closer to the Full-shell
550 model when compared with the Macro (Built-in) model, particularly in the web elements. The rate
551 of convergence is also important for validating the implementation of the proposed WIKC method
552 and to assess the overall computational effort required. To this end, a plot of the total number of
553 iterations in the analysis with respect to the applied torque is provided in Fig. 10. This figure shows
554 that the convergence rate of the Macro (Warping) model is comparable to the Full-shell model up
555 to the point of divergence between these models at around 12 kN-m.

Case Study 2: Interior Subassembly Results

The overall subassembly behavior in terms of story drift ratio (SDR = column tip displacement / initial column length) and column tip load is shown in Fig. 11. The Full-shell model is able to capture reasonably well the pre- and post-peak behavior of the subassembly, note that the relative error in the maximum absolute column tip load is around 2 % between the Full-shell and Test Data. There is also good agreement between the Full-shell model unloading stiffness and the test data prior to the last cycle of loading, indicating that the Full-shell model is able to capture the progression of local buckling in the RBS region and twisting of the beams and column. This observation is reflected by the apparent match between the post-test deformed shapes found in the Full-shell model and the experiment itself, as shown in Fig. 12. Certain features of the test data are not replicated by the model (e.g., the apparent stiffening of the test response in cycles after 2 %SDR), although, this is attributed to boundary condition effects that are not fully captured by the model, as this particular test was stopped after the cycles to 5 %SDR due to damage in the lateral support system (Engelhardt et al. 2000). The angle of twist predicted by the Full-shell model at the column bottom is approximately 0.12 rad at the final excursion to -5 %SDR, and the beam angle of twist is approximately 0.22 rad (see also Fig. 12), indicating that torsional effects are expected to be significant. The Full-shell model is also able to capture the panel zone behavior of the subassembly, as show in Fig. 13a, although the peak shear rotation is slightly overestimated.

The Macro (Built-in) and Macro (Warping) models are compared with the Full-shell model in Figs. 11b and 11c. Both models predict reasonably well the Full-shell model's response, although, the Macro (Built-in) model overestimates the overall unloading/reloading stiffness after the initiation of beam twisting due to the increased torsional stiffness of the beams and column. Additionally, the Macro (Warping) model is able to represent the Full-shell model panel zone behavior, as indicated in Fig. 13b. Note that results for the Macro (Lin. Warping) model are not shown for this case, as convergence issues were experienced for this model due to the linear coupling formulation.

The memory and DOF requirements for Case Study 2 are provided in Fig. 14. This figure plots the memory required by the analyses normalized by the requirement of the Full-shell model, and

583 similarly with the total DOFs in the models. Results are shown for the Macro (Warping) model
584 only, however, they are very similar for the Macro (Built-in) model barring differences of around
585 1 % in the DOF and memory requirements that may be attributed to the use of a user subroutine in
586 Abaqus v6.14. For Case 2, a reduction in the number of DOFs required is around 55 %, and the
587 reduction in memory required is around 48 %.

588 **Case Study 3: Quasi-Static Collapse-Consistent Loading of First-story Column Results**

589 Column reaction moments at the base without the second-order contribution, M_{col} , are reported
590 herein. For clarity, $M_{col} = M_{total} - M_{PD}$, where M_{total} is the total base reaction moment, and
591 $M_{PD} = u_y F_z$ is the second-order moment about the column base. The SDR is computed as
592 $SDR = (u_y^{top} - u_y^{base})/L_0$, and axial shortening is reported as a percent of the initial length, u_z/L_0 .

593 The column moment vs. story drift ratio (SDR) is plotted in Fig. 15 including the test data and
594 comparisons between the Full-shell model and different macro models. Relative error between the
595 maximum absolute moment of the Full-shell and test data is around 7 %, indicating the models'
596 ability to capture the initial flexural yielding behavior of the steel material and initiation of local
597 buckling in the column. Furthermore, agreement of the loading/unloading stiffness between the
598 Full-shell results and Test Data indicates that the progression of local buckling is reasonably well
599 captured by the Full-shell model. Computation of the column response is also validated through
600 the deformed shape of the column models at the excursion at +10 %SDR with a photograph from
601 the test at the same point in Figures 16a and 16b. Agreement between the deformed shapes and the
602 test results is notable. The maximum angle of twist observed in this test and finite element analyses
603 is around 0.10 rad in the last loading excursion, although the effect of torsion is not significant in
604 this case as the problem is dominated by local buckling (Elkady and Lignos 2018a).

605 Each of the macro modeling options are also compared individually with the Full-shell model
606 in Fig. 15. In this case that the strength/stiffness deterioration is dominated by local buckling,
607 there are no significant differences between the Full-shell and macro model responses in terms of
608 moment-rotation throughout the entire loading history, regardless of the coupling method. Despite
609 the agreement in overall component behavior, the stress at the interface may be significantly in error

610 with the linear coupling method, as noted in Fig. 16e. The number of DOFs in the model and the
611 computer memory demands are extracted from information provided by the Abaqus analysis and
612 presented in Fig. 14 above the label “Case 3”. A savings of around 60 % in the number of DOFs is
613 obtained by the macro models since around 2/3 of the total length is modeled with beam-column
614 elements, and the memory savings is around 80 % in this case (see Fig. 14).

615 **Case Study 4: Column Nonlinear Response History Analysis Results**

616 Modal frequencies determined through eigenvalue analysis of the four W24X94 models are
617 provided in Table 5, Mode 1 is the primary lateral mode of deformation, and Mode 3 is the twisting
618 mode provided for comparison purposes. In all cases the first mode period is approximately equal
619 to 1.5 s validating the assumed mass. The Mode 3 frequency of the Macro (Built-in) model is
620 around 50 % larger than the Full-shell frequency because of the difference in elastic torsional
621 stiffness. Note that the linear WIKC model’s Mode 1 and Mode 3 frequencies are consistent with
622 the Full-shell model.

623 The SDR, column base moment, and axial displacement as a percentage of the initial column
624 length are provided with respect to the applied ground motion time in Fig. 17. The point at which
625 the column loses load carrying capacity is evident as the slopes of the SDR and axial displacement
626 approach $-\infty$. The Full-shell model point of collapse is reasonably well computed by the Macro
627 (Warping) model, as evident in Fig. 17, however, the same cannot be said for the Macro (Built-in)
628 model.

629 In contrast with Case Study 3, divergence in the response of the Macro (Built-in) and Macro
630 (Lin. Warping) models from the Full-shell model is found in Case Study 4. Divergence at the
631 point indicated in Fig. 17 stems from the computation of different buckling modes: the W24X94
632 Macro (Built-in) and Macro (Lin. Warping) models deforms in a primarily local buckling mode,
633 while the Full-shell and Macro (Warping) model have a coupled buckling response, as shown in
634 Fig. 18. Differences in the buckling modes subsequently leads to differences in the column base
635 moment responses, as highlighted in Fig. 17, while the Macro (Warping) model agrees well with
636 the Full-shell model until near the point of the loss of load carrying capacity. The W24X94 column

637 Full-shell model stress distribution is also reasonably well predicted by the Macro (Warping)
638 model as indicated by comparing the von Mises stress contours in Fig. 18. Computational resource
639 demands of the column models are summarized in Fig. 14 with respect to the Full-shell model.
640 The number of DOFs are reduced by around 40 % are obtained for the W24X94 macro models
641 compared to the Full-shell model, and the memory requirements are reduced by around 75 %.

642 **DISCUSSION OF RESULTS**

643 **Macro Model Accuracy**

644 Case studies investigated in this paper show that, as long as the coupling between beam-column
645 and continuum elements can account for all relevant mechanical phenomena, the component macro
646 models represent well the Full-shell model. This statement is made with regards to parameters
647 that have been identified as critical in collapse simulations of steel frame buildings (Ibarra and
648 Krawinkler 2005), such as a component's: pre-peak stiffness, peak strength, and post-peak stiffness.
649 These results indicate that the macro models can replicate the Full-shell model's initiation and
650 progression of local and lateral-torsional buckling, as well as the progression of axial shortening.
651 This is true even in the complex case of coupled local and lateral-torsional buckling. Therefore,
652 component macro models can be used to address the limitations outlined in the introduction for
653 concentrated and distributed plasticity approaches provided that a suitable coupling method is used,
654 and the component deformation is within the range of its constitutive elements.

655 More specifically, from the cases investigated, there is little-to-no difference between the differ-
656 ent coupling methods when computing the pre-peak response and initiation of *local* instabilities in
657 wide-flange beam-column components subjected to axial load and/or lateral drift demands. How-
658 ever, the influence of warping in the constraint formulation is paramount in the case of nonuniform
659 torsion and coupled buckling mechanisms due to the increase in torsional stiffness found using the
660 Abaqus v6.14 built-in coupling. The stiffness increase is a result of the warping-fixed boundary
661 enforced on the continuum domains, as seen in the results of case studies, as well as the Mode 3
662 frequency in Table 5 for the W24X94 column. The increase in torsional stiffness decreases the
663 member's proclivity to LTB, this in-turn leads to the divergence in buckling modes between the

664 Macro (Built-in) and Macro (Warping) models in the W24X94 dynamic analyses, as shown in
665 Fig. 7. Differences of stiffness in the descending portion of the post-peak response, such as the
666 ones shown in Fig. 11b for the Macro (Built-in) model, are critical in collapse simulations (Ibarra
667 and Krawinkler 2005), alternatively, this stiffness is well predicted by the Macro (Warping) model
668 in Fig. 11c. An initial recommendation based on the results presented in this paper is that a
669 warping-inclusive coupling method should be used for beam-column components that have a sig-
670 nificant torsional load, or that have a normalized LTB slenderness $\bar{\lambda}_{LT} > 0.4$ that is considered
671 susceptible to inelastic LTB according to CEN (2005).

672 From an accuracy point of view, it appears that if torsion is not dominant in the component
673 response and there is no coupled buckling, the choice of coupling method is not influential in
674 the column post-peak region. This result suggests that including warping in the coupling can be
675 neglected for beam-column components if $\bar{\lambda}_{LT} \leq 0.4$. Furthermore, linear coupling methods are
676 found to be acceptable under the following conditions: local buckling is dominant in the member
677 response, the lateral deformation is below 10 %SDR, and the angle of twist does not exceed 0.10 rad.
678 If torsion is dominant, the linear coupling method may be used as long as the angle of twist does
679 not exceed 0.05 rad (see Fig. 8b). The linear WIKC method can also be employed in eigenvalue
680 analyses, as supported by the results of the frequency analysis in Table 5.

681 **Macro Model Computational Efficiency**

682 Results of the computational resource metrics shown in Fig. 14 illustrate that the number of
683 DOFs in the macro models are reduced in approximate proportion to the ratio L_{Ω_1}/L for single
684 components. For instance, the number of DOFs are approximately 2/3 for the W24X94 macro
685 models compared to the Full-shell model in Fig. 14 since 1/3 of the length is modeled with beam-
686 column elements. This ratio of 2/3 is increased for the W24X94 analyses owing to the increased
687 beam-column domain length. The memory savings are expected to be larger than the DOF savings,
688 although the relationship is not clear, as elements of the square matrices need to be saved in addition
689 to state variables for each element. For these reasons, the memory reduction using component macro
690 models in Case Study 2 is less pronounced than the other cases, potentially due to the increased

691 complexity and number of constraints present in this model to form the subassembly.

692 In the context of frame analysis, additional computational savings can be gained if the macro
693 model approach is applied selectively depending on the desired level of modeling fidelity and
694 available computational resources. For instance, the macro model approach could be useful to
695 model the torsion induced on columns due to buckling of beams with RBS connections, as well
696 as first-story columns that experience deterioration in capacity-designed MRFs. This selective
697 approach focuses the computational effort where it is most useful, while lower fidelity component
698 models (i.e., concentrated and distributed plasticity approaches) can be used elsewhere in the
699 structural model. Furthermore, the number of iterations required for convergence of the Macro
700 (Warping) model appears similar to the Full-shell and Macro (Built-in) models, see Fig. 10.
701 Therefore, the reduced number of DOFs in macro models is expected to also reduce the required
702 CPU time compared to full-shell models. Finally, the linear WIKC method may lead to issues
703 with global convergence in certain nonlinear problems. The linear WIKC method is, therefore, not
704 computationally advantageous in these cases, and is recommended only if the nonlinear method is
705 unavailable.

706 **Limitations**

707 The following limitations uncovered through this study are stated:

- 708 • Residual stresses have not been included in the beam-column elements used in this study.
709 This limitation could be addressed using a beam-column element formulation such as in
710 [Lamarche and Tremblay \(2011\)](#). Residual stresses may influence the Wagner constant
711 ([Trahair 1993](#); [de Castro e Sousa and Lignos 2017](#)), that in-turn, could substantially reduce
712 the torsional stiffness of beam-columns. This reduction may be critical for slender members
713 as it further increases their susceptibility to LTB.
- 714 • The limitation of using beam-column elements is that local deformations cannot be captured
715 in the beam-column domains, therefore, the length of the continuum domains need to be
716 chosen appropriately *a priori*. This challenge has yet to be addressed because the extent

717 of local instabilities in the member depends on the primary mode of deterioration (e.g.,
718 local buckling, lateral-torsional buckling, flexural buckling) that is ultimately influenced
719 by the member geometry, material properties, initial imperfections, loading, and boundary
720 conditions.

- 721 • The results presented herein are for shell elements in the continuum domain only, solid
722 elements have not yet been investigated by the authors. However, the proposed coupling
723 method is valid for these elements since only the displacement DOFs of the continuum
724 domain are coupled with the beam-column element domain.

725 **CONCLUSIONS**

726 Continuum finite element models address the limitations in available concentrated and dis-
727 tributed plasticity component models for steel wide-flange beam-columns, however, they may be
728 computationally expensive in the context of earthquake engineering analysis. Mixed-dimension
729 macro models employing 1D beam-column and 2D/3D continuum elements are promising to re-
730 duce this computational expense. A review of existing coupling methods highlights that there is a
731 need for a multi-point constraint method that also incorporates torsion warping. In this paper, we
732 propose a warping-inclusive kinematic coupling (WIKC) formulation to transfer warping deforma-
733 tions between the beam-column and continuum element domains. The beam-shell macro models
734 used in this study reduce the model degrees-of-freedom by up-to around 60 % and the computa-
735 tional memory requirement by up-to around 80 % compared to their full-shell counterparts, while
736 retaining the solution fidelity of full-continuum finite element models even for coupled local and
737 lateral-torsional buckling.

738 The main conclusions drawn from this paper with respect to steel wide-flange beam-columns
739 and subassemblies are as follows:

- 740 • Including warping in the coupling formulation may be critical in accurately estimating the
741 full-continuum model failure mode and, therefore, should be included for general use. This
742 is especially true for components subjected to nonuniform torsion, or that are susceptible to

743 coupled local and lateral-torsional instabilities, i.e., if $\bar{\lambda}_{LT} > 0.4$.

- 744 • A nonlinear, finite-rotation constraint formulation appears to be necessary for nonlinear
745 problems, and there does not appear to be any computational advantages offered by the
746 linear coupling method. Linear, small-rotation coupling methods appear to be acceptable
747 for eigenvalue analyses, as well as problems not dominated by torsion if: (i) LTB is not
748 critical, (ii) the angle of twist is less than 0.10 rad, and (iii) the column drift is below 10 %.
749 If twisting is the dominant mode of deformation, the angle of twist should remain below
750 0.05 rad if a linear coupling method is employed.
- 751 • The macro model approach leads to a reduction in the DOFs and memory usage proportional
752 to the ratio of the beam-column element domain length to the total component length. The
753 macro model approach does not appear to negatively affect the rate of convergence compared
754 to the full-continuum model, therefore, the computational time savings are expected to be a
755 function of the DOF reduction.

756 Macro model parameters (e.g., proportion of continuum domain, mesh discretization, imper-
757 fections, etc.) need to be calibrated in a future study based on the member geometry, boundary
758 conditions, material properties, and loading. Such guidelines will allow for the practical use of
759 component macro models in frame simulations.

760 DATA AVAILABILITY

- 761 • Some or all data, models, or code generated or used during the study are available in a
762 repository or online in accordance with funder data retention policies. This includes: the
763 code for the proposed coupling method and imperfection generation (Hartloper 2020); and
764 the code used to generate the Voce-Chaboche material model properties (de Castro e Sousa
765 et al. 2019).
- 766 • Some or all data, models, or code that support the findings of this study are available from
767 the corresponding author upon reasonable request. This includes: the finite element models
768 used in the case studies.

769 **ACKNOWLEDGEMENTS**

770 The Authors sincerely thank Professor Michael Engelhardt from the University of Texas at
771 Austin for allowing for the use of Fig. 12 and providing the experimental data for the DBBW
772 subassembly. The Authors also sincerely thank Professor Ahmed Elkady from the University of
773 Southampton for allowing use of Figs. 7c/16a and providing the experimental data from specimen
774 C5. This study is based on work supported by EPFL and by the Swiss National Science Foundation
775 (Project No. 200021_188476) for the first author, and an EPFL internal grant for the second author.
776 The financial support is gratefully acknowledged. Any opinions, findings, and conclusions or
777 recommendations expressed in this paper are those of the authors and do not necessarily reflect the
778 view of sponsors.

NOTATION

The following symbols are used in this paper:

$\mathbf{A}_1, \mathbf{A}_2$ = constraint coefficient matrices;

b_f = flange width;

$(\cdot)^b$ = beam quantity;

$(\cdot)^c$ = continuum quantity;

d = wide-flange section depth;

f = constraint equations for a continuum node;

\mathbf{I} = 3×3 identity matrix;

L = member length;

\mathbf{l} = link vector;

$\mathbf{n}_1, \mathbf{n}_2$ = cross-sectional plane vectors;

\mathbf{R} = rotation matrix;

\mathbf{t} = cross-sectional normal vector;

t_f = flange thickness;

t_w = web thickness;

\mathbf{u} = nodal displacement vector;

\mathbf{v} = nodal initial imperfection vector;

w = warping DOF;

\mathbf{x} = nodal position vector;

$\delta(\cdot)$ = infinitesimal quantity;

Γ = beam-continuum interface;

ξ = distance along \mathbf{n}_1 axis;

$\boldsymbol{\theta}$ = infinitesimal nodal rotation vector;

η = distance along \mathbf{n}_2 axis;

ψ = warping function;

ϕ = nodal rotation vector;

ζ = distance along n_3 axis;

782

Ω_1 = beam-column element domain;

Ω_2 = continuum element domain; and

$[(\cdot)]_x$ = matrix representation of cross-product.

REFERENCES

- AISC (2016). "Specification for structural steel buildings." *ANSI/AISC 360-16*, American Institute of Steel Construction, Chicago, Illinois, United States.
- Araújo, M., Macedo, L., and Castro, J. M. (2017). "Evaluation of the rotation capacity limits of steel members defined in EC8-3." *Journal of Constructional Steel Research*, 135, 11–29.
- ASTM (2016). "Standard Specification for General Requirements for Rolled Structural Steel Bars, Plates, Shapes, and Sheet Piling." *A6/A6M-16a*, ASTM International, West Conshohocken, PA, USA.
- CEN (1993). "Structural steel I and H sections. Tolerances on shape and dimensions.." *EN 10034:1993*, European Committee for Standards, Brussels, Belgium.
- CEN (2005). "Eurocode 3: Design of steel structures - Part 1-1: General rules and rules for buildings." *EN 1993-1-1*, European Committee for Standardization, Brussels, Belgium.
- Chavan, K. S. and Wriggers, P. (2004). "Consistent coupling of beam and shell models for thermo-elastic analysis." *International Journal for Numerical Methods in Engineering*, 59(14), 1861–1878.
- Chen, W.-F. and Atsuta, T. (2008). *Theory of Beam-Columns Volume 2: Space Behavior and Design*. J. Ross Publishing, Fort Lauderdale, FL, USA.
- Cravero, J., Elkady, A., and Lignos, D. G. (2020). "Experimental Evaluation and Numerical Modeling of Wide-Flange Steel Columns Subjected to Constant and Variable Axial Load Coupled with Lateral Drift Demands." *Journal of Structural Engineering*, 146(3), 04019222.
- Dassault Systèmes (2014). *Abaqus Standard and Abaqus Documentation for Version 6.14*. Dassault Systèmes Simulia Corp., Providence, RI, USA.
- de Castro e Sousa, A., Hartloper, A. R., and Lignos, D. G. (2019). "RESSPyLab version 1.0 - Python tools for structural steel research, <<https://pypi.org/project/RESSPyLab/>>.
- de Castro e Sousa, A., Hartloper, A. R., and Lignos, D. G. (2020a). "Cyclic metal plasticity model parameters with limited information: A constrained optimization approach (submitted)." *Journal of Engineering Mechanics*.

810 de Castro e Sousa, A. and Lignos, D. G. (2017). “Residual stress measurements of European hot-
811 rolled I-shaped steel profiles.” *Technical Report 231302*, Resilient Steel Structures Laboratory,
812 École Polytechnique Fédérale de Lausanne (EPFL), Lausanne, Switzerland.

813 de Castro e Sousa, A., Suzuki, Y., and Lignos, D. (2020b). “Consistency in Solving the Inverse
814 Problem of the Voce-Chaboche Constitutive Model for Plastic Straining.” *Journal of Engineering*
815 *Mechanics*, 146(9), 04020097.

816 Deierlein, G. G. and Zsarnóczy, A. (2019). “State-of-Art in Computational Simulation for Natural
817 Hazards Engineering.” *Report No. 2019-01*, NHERI SimCenter, Richmond, California, USA.

818 Di Re, P., Addessi, D., and Filippou, F. C. (2018). “Mixed 3D Beam Element with Damage Plasticity
819 for the Analysis of RC Members under Warping Torsion.” *Journal of Structural Engineering*,
820 144(6), 04018064.

821 Elkady, A. (2016). “Collapse Risk Assessment of Steel Moment Resisting Frames Designed with
822 Deep Wide-Flange Columns in Seismic Regions.” PhD Thesis, McGill University, Montreal,
823 Quebec, Canada.

824 Elkady, A., Güell, G., and Lignos, D. G. (2020). “Proposed methodology for building-specific
825 earthquake loss assessment including column residual axial shortening.” *Earthquake Engineering*
826 *& Structural Dynamics*, 49(4), 339–355.

827 Elkady, A. and Lignos, D. G. (2015a). “Analytical investigation of the cyclic behavior and plastic
828 hinge formation in deep wide-flange steel beam-columns.” *Bulletin of Earthquake Engineering*,
829 13(4), 1097–1118.

830 Elkady, A. and Lignos, D. G. (2015b). “Effect of gravity framing on the overstrength and col-
831 lapse capacity of steel frame buildings with perimeter special moment frames.” *Earthquake*
832 *Engineering & Structural Dynamics*, 44(8), 1289–1307.

833 Elkady, A. and Lignos, D. G. (2018a). “Full-Scale Testing of Deep Wide-Flange Steel Columns
834 under Multiaxis Cyclic Loading: Loading Sequence, Boundary Effects, and Lateral Stability
835 Bracing Force Demands.” *Journal of Structural Engineering*, 144(2), 04017189.

836 Elkady, A. and Lignos, D. G. (2018b). “Improved Seismic Design and Nonlinear Modeling Rec-

837 ommendations for Wide-Flange Steel Columns.” *Journal of Structural Engineering*, 144(9),
838 04018162.

839 Engelhardt, M. D., Fry, G., Jones, S., Venti, M., and Holliday, S. (2000). “Behavior and design of
840 radius-cut, reduced beam section connections.” *Report No. SAC/BD-00/17*, SAC Joint Venture, a
841 partnership of the Structural Engineers Association of California, Applied Technology Council,
842 and California Universities for Research in Earthquake Engineering, Sacramento, California,
843 United States.

844 Farwell, C. R. and Galambos, T. V. (1969). “Nonuniform Torsion of Steel Beams in Inelastic
845 Range.” *Journal of the Structural Division*, 95(12), 2813–2830.

846 FEMA (2000). “State of the Art Report on Connection Performance.” *Report No. 355D*, Federal
847 Emergency Management Agency, Washington, DC, United States.

848 FEMA (2009). “Quantification of Building Seismic Performance Factors.” *P-695*, Federal Emer-
849 gency Management Agency, Washington, DC, USA.

850 Fogarty, J. and El-Tawil, S. (2015). “Collapse Resistance of Steel Columns under Combined Axial
851 and Lateral Loading.” *Journal of Structural Engineering*, 142(1).

852 Galambos, T. V. (1998). *Guide to Stability Design Criteria for Metal Structures*. John Wiley &
853 Sons, New York, NY, USA, fifth edition.

854 Gantes, C. J. and Fragkopoulos, K. A. (2010). “Strategy for numerical verification of steel structures
855 at the ultimate limit state.” *Structure and Infrastructure Engineering*, 6(1-2), 225–255.

856 Haaijer, G. (1956). “Local buckling of wf shapes in the plastic range.” PhD. Thesis, Lehigh
857 University, Bethlehem, Pennsylvania, USA.

858 Hajjar, J. F., Schiller, P. H., and Molodan, A. (1998). “A distributed plasticity model for concrete-
859 filled steel tube beam-columns with interlayer slip.” *Engineering Structures*, 20(8), 663–676.

860 Hartloper, A. R. (2020). “WIKC: Warping-Inclusive Kinematic Coupling Definition and Pre-
861 processing, <<https://github.com/ahartloper/WIKC>>.

862 Hartloper, A. R. and Lignos, D. G. (2019). “Measurement and Identification of Imperfections
863 in Steel Wide-flange Cross-sections Using Point Cloud Data.” *Report No. 264781*, Resilient

864 Steel Structures Laboratory, École Polytechnique Fédérale de Lausanne (EPFL), Lausanne,
865 Switzerland.

866 Hill, H. N. (1940). “Chart for Critical Compressive Stress of Flat Rectangular Plates.” *Technical Note*
867 773, National Advisory Committee for Aeronautics. Langley Aeronautical Lab., Washington,
868 D.C., United States.

869 Ho, R. J., Meguid, S. A., Zhu, Z. H., and Sauv e, R. G. (2010). “Consistent element coupling in
870 nonlinear static and dynamic analyses using explicit solvers.” *International Journal of Mechanics*
871 *and Materials in Design*, 6(4), 319–330.

872 Ibarra, L. F. and Krawinkler, H. (2005). “Global collapse of frame structures under seismic excita-
873 tions.” *Report No. 152*, The John A. Blume Earthquake Engineering Research Center, Stanford
874 University, Stanford, California, United States.

875 Ibarra, L. F., Medina, R. A., and Krawinkler, H. (2005). “Hysteretic models that incorporate strength
876 and stiffness deterioration.” *Earthquake engineering & structural dynamics*, 34(12), 1489–1511.

877 Imanpour, A., Tremblay, R., Davaran, A., Stoakes, C. D., and Fahnestock, L. A. (2016). “Seismic
878 Performance Assessment of Multitiered Steel Concentrically Braced Frames Designed in Ac-
879 cordance with the 2010 AISC Seismic Provisions.” *Journal of Structural Engineering*, 142(12),
880 04016135.

881 Kalochairetis, K. E. and Gantes, C. J. (2011). “Numerical and analytical investigation of collapse
882 loads of laced built-up columns.” *Computers & Structures*, 89(11), 1166–1176.

883 Koczubiej, S. and Cicho n, C. (2014). “Global static and stability analysis of thin-walled structures
884 with open cross-section using FE shell-beam models.” *Thin-Walled Structures*, 82, 196–211.

885 Kostic, S. M. and Filippou, F. C. (2012). “Section Discretization of Fiber Beam-Column Elements
886 for Cyclic Inelastic Response.” *Journal of Structural Engineering*, 138(5), 592–601.

887 Krawinkler, H., Zareian, F., Medina, R. A., and Ibarra, L. F. (2006). “Decision support for con-
888 ceptual performance-based design.” *Earthquake Engineering & Structural Dynamics*, 35(1),
889 115–133.

890 Krishnan, S. (2010). “Modified Elastofiber Element for Steel Slender Column and Brace Modeling.”

891 *Journal of Structural Engineering*, 136(11).

892 Lamarche, C.-P. and Tremblay, R. (2011). “Seismically induced cyclic buckling of steel columns
893 including residual-stress and strain-rate effects.” *Journal of Constructional Steel Research*, 67(9),
894 1401–1410.

895 Le Corvec, V. (2012). “Nonlinear 3D frame element with multi-axial coupling under considerations
896 of local effects.” Ph.D. thesis, University of California, Berkeley, Berkeley, CA, USA.

897 Lignos, D. G., Hartloper, A. R., Elkady, A., Deierlein, G. G., and Hamburger, R. O. (2019). “Pro-
898 posed Updates to the ASCE 41 Nonlinear Modeling Parameters for Wide-Flange Steel Columns
899 in Support of Performance-based Seismic Engineering.” *Journal of Structural Engineering*,
900 145(9), 04019083.

901 Lignos, D. G. and Krawinkler, H. (2011). “Deterioration Modeling of Steel Components in Support
902 of Collapse Prediction of Steel Moment Frames under Earthquake Loading.” *Journal of Structural
903 Engineering*, 137(11), 1291–1302.

904 Lignos, D. G. and Krawinkler, H. (2013). “Development and utilization of structural component
905 databases for performance-based earthquake engineering.” *Journal of Structural Engineering*,
906 139(8), 1382–1394.

907 Liu, H. (2016). “Modeling of frame structures undergoing large deformations and large rotations.”
908 PhD Thesis, Purdue University, West Lafayette, Indianapolis, USA.

909 Mari, A. R. (1984). “Nonlinear geometric material and time dependent analysis of three dimensional
910 reinforced and prestressed concrete frames.” PhD Thesis, University of California, Berkeley,
911 Berkeley, California, USA.

912 Mathur, K., Fahnestock, L. A., Okazaki, T., and Parkolap, M. J. (2012). “Impact of Residual
913 Stresses and Initial Imperfections on the Seismic Response of Steel Moment Frames.” *Journal
914 of Structural Engineering*, 138(7), 942–951.

915 McCune, R. W., Armstrong, C. G., and Robinson, D. J. (2000). “Mixed-dimensional coupling
916 in finite element models.” *International Journal for Numerical Methods in Engineering*, 49(6),
917 725–750.

918 Miyamura, T., Yamashita, T., Akiba, H., and Ohsaki, M. (2015). “Dynamic FE simulation of
919 four-story steel frame modeled by solid elements and its validation using results of full-scale
920 shake-table test.” *Earthquake Engineering & Structural Dynamics*, 44(9), 1449–1469.

921 Monaghan, D. J., Doherty, I. W., Mc Court, D., and Armstrong, C. G. (1998). “Coupling 1D Beams
922 to 3D Bodies.” *Proceedings of the 7th International Meshing Roundtable*, Dearborn, Michigan,
923 USA, Sandia National Lab.

924 NIST (2010). *Evaluation of the FEMA P-695 Methodology for Quantification of Building Seismic*
925 *Performance Factors*. US Department of Commerce, Engineering Laboratory, National Institute
926 of Standards and Technology, Gaithersburg, Maryland, USA.

927 Ozkula, G., Harris, J., and Uang, C.-M. (2017). “Observations from Cyclic Tests on Deep, Wide-
928 Flange Beam-Columns.” *Engineering Journal*, 54(1), 45–59.

929 Pi, Y. L. and Trahair, N. S. (1995). “Inelastic torsion of steel I-beams.” *Journal of structural*
930 *Engineering*, 121(4), 609–620.

931 Rodrigues, O. (1840). “Des lois géométriques qui régissent les déplacements d’un système solide
932 dans l’espace, et de la variation des coordonnées provenant de ces déplacements considérés
933 indépendamment des causes qui peuvent les produire.” *Journal de mathématiques pures et*
934 *appliquées*, 5, 62.

935 Sadeghian, V., Kwon, O.-S., and Vecchio, F. (2018). “Modeling Beam-Membrane Interface in
936 Reinforced Concrete Frames.” *ACI Structural Journal*, 115(3).

937 Shim, K. W., Monaghan, D. J., and Armstrong, C. G. (2002). “Mixed Dimensional Coupling in
938 Finite Element Stress Analysis.” *Engineering with Computers; Heidelberg*, 18(3), 241–252.

939 Simo, J. C. and Vu-Quoc, L. (1991). “A Geometrically-exact rod model incorporating shear and
940 torsion-warping deformation.” *International Journal of Solids and Structures*, 27(3), 371–393.

941 Sivaselvan, M. and Reinhorn, A. M. (2000). “Hysteretic Models for Deteriorating Inelastic Struc-
942 tures.” *Journal of Engineering Mechanics*, 126(6), 633–640.

943 Sivaselvan, M. V. and Reinhorn, A. M. (2002). “Collapse Analysis: Large Inelastic Deformations
944 Analysis of Planar Frames.” *Journal of Structural Engineering*, 128(12), 1575–1583.

945 Song, H. (2010). “Rigorous joining of advanced reduced-dimensional beam models to three-
946 dimensional finite element models.” PhD. Thesis, Georgia Institute of Technology, Atlanta,
947 Georgia, USA.

948 Spacone, E., Filippou, F. C., and Taucer, F. F. (1996). “Fibre Beam–Column Model for Non-Linear
949 Analysis of R/C Frames: Part I. Formulation.” *Earthquake Engineering & Structural Dynamics*,
950 25(7), 711–725.

951 Sreenath, S., Saravanan, U., and Kalyanaraman, V. (2011). “Beam and shell element model for
952 advanced analysis of steel structural members.” *Journal of Constructional Steel Research*, 67(12),
953 1789–1796.

954 Stoakes, C. D. and Fahnestock, L. A. (2016). “Strong-Axis Stability of Wide Flange Steel Columns
955 in the Presence of Weak-Axis Flexure.” *Journal of Structural Engineering*, 142(5), 04016004.

956 Suzuki, Y. and Lignos, D. G. (2015). “Large Scale Collapse Experiments of Wide Flange Steel
957 Beam-Columns.” *8th International Conference on Behaviour of Steel Structures in Seismic Areas*,
958 Vol. 4, Shanghai, China.

959 Suzuki, Y. and Lignos, D. G. (2020). “Development of collapse-consistent loading protocols for
960 experimental testing of steel columns.” *Earthquake Engineering & Structural Dynamics*, 49(2),
961 114–131.

962 Tada, M., Tamai, H., Ohgami, K., Kuwahara, S., and Horimoto, A. (2008). “Analytical simulation
963 utilizing collaborative structural analysis system.” *Proceedings of 14th World Conference on*
964 *Earthquake Engineering*.

965 Trahair, N. S. (1993). *Flexural-Torsional Buckling of Structures*. CRC Press, Boca Raton, Florida,
966 USA (July).

967 Vamvatsikos, D. and Cornell, C. A. (2002). “Incremental dynamic analysis.” *Earthquake Engineer-*
968 *ing & Structural Dynamics*, 31(3), 491–514.

969 Wagner, W. and Gruttmann, F. (2002). “Modeling of shell-beam transitions in the presence of finite
970 rotations.” *Computer Assisted Mechanics and Engineering Sciences*, 9(3), 405–418.

971 Whyte, C. A., Mackie, K. R., and Stojadinovic, B. (2016). “Hybrid Simulation of Thermomechan-

972 ical Structural Response.” *Journal of Structural Engineering*, 142(2), 04015107.
973 Wu, T.-Y., El-Tawil, S., and McCormick, J. (2018). “Seismic Collapse Response of Steel Moment
974 Frames with Deep Columns.” *Journal of Structural Engineering*, 144(9), 04018145.
975 Ziemian, R. D. (2010). *Guide to Stability Design Criteria for Metal Structures*. John Wiley & Sons,
976 Inc., New Jersey, USA, sixth edition.

977

List of Tables

978 1 Overview of the case studies. 43

979 2 Wide-flange member geometry used in the analysis cases. 44

980 3 Case study macro model and imperfection parameters. 45

981 4 Case study Voce-Chaboche material model parameters. 46

982 5 Frequencies for selected modes of the W24X94 column. 47

TABLE 1. Overview of the case studies.

Case Study ID	Description	Component(s)	Material	Equilibrium Path
Case 1	Nonuniform torsion	Beam: $6 \times 6-25$	A36	Stable
Case 2	Interior subassembly	Column: W14X398, Beam: W36X150	A572 Gr. 50	Unstable
Case 3	First-story column, quasi-static loading	Column: W24X146	A992 Gr. 50	Unstable
Case 4	First-story column, dynamic loading	Column: W24X94	A992 Gr. 50	Unstable

TABLE 2. Wide-flange member geometry used in the analysis cases.

Case	Section	d [mm]	b_f [mm]	t_f [mm]	t_w [mm]	L_b [mm]	$b_f/2t_f$ -	h/t_w -	L_b/r_y -	$\bar{\lambda}_{LT}^b$ -	L_r [m]
1	6 × 6-25	152	151	12.2	8.0	1930	6.20	16.0	50	0.20	10.7
2	W14X398	465	442	72.4	45.0	3708	2.92	6.44	34	0.15	41.8
2	W36X150	912	305	23.9	15.9	3962	6.37	51.9	63	0.31	7.7
3	W24X146 ^a	627	325	27.1	17.6	3900	5.92	33.2	51	0.29	10.2
4	W24X94	617	230	22.2	13.1	5500	5.18	41.9	109	0.50	6.4

^a: measured d, b_f, t_f, t_w . ^b: $\bar{\lambda}_{LT} = \sqrt{Z_x f_y / M_{cr}}$

$$M_{cr} = C_1 \pi^2 E I_y / (k_y L)^2 \sqrt{(k_y / k_w)^2 I_w / I_y + (k_y L)^2 G I_t / (\pi^2 E I_y)}, C_1 = 2.55, k_y = 0.5, k_w = 1.0$$

TABLE 3. Case study macro model and imperfection parameters.

Case Study ID	L_{Ω_2} [mm]	Δ_{shell} [mm]	Shell Type	N_{beam}	Beam Type	L_{bw} [mm]	θ_{twist} [%rad]
Case 1	482.5	<20	S4R	8	B32OS	-	-
Case 2, column	1700	<50	S4R	4	B31OS	-	-
Case 2, beams	1300	<25 ^a	S4R	6	B31OS	686	-
Case 3	800	<25	S4R	4	B31OS	752	0.05
Case 4	1650	<25	S4R	4	B31OS	740	0.6

^a: <25 mm in the RBS region, <50 mm elsewhere.

TABLE 4. Case study Voce-Chaboche material model parameters.

Material	E [GPa]	$\sigma_{y,0}$ [MPa]	Q_∞ [MPa]	b -	C_1 [MPa]	γ_1 -	C_2 [MPa]	γ_2 -
A572 Gr.50 ^a	207.34	352.01	61.60	8.96	2305.55	20.15	-	-
A992 Gr.50 Flange ^b	179.75	318.47	100.72	8.00	11608.17	145.22	1026.33	4.68
A992 Gr.50 Web ^b	182.97	339.18	77.52	9.29	8716.08	118.47	1182.05	5.22

^a: calibrated as a part of this study, ^b: from de Castro e Sousa et al. (2020).

TABLE 5. Frequencies for selected modes of the W24X94 column.

Model	Mode 1 (Lateral)		Mode 3 (Twisting)	
	Freq. [Hz]	E_{fs} [%]	Freq. [Hz]	E_{fs} [%]
Full-shell	0.667	-	1094	-
Macro (Built-in)	0.668	0.15	1661	51.83
Macro (Warping)	0.668	0.15	1109	1.37
Macro (Lin. Warping)	0.668	0.15	1118	2.19

$E_{fs} = (\text{Full-shell} - \text{Macro}) / \text{Full-shell}$.

983 **List of Figures**

984 1 Mixed-dimension component macro model concept for wide-flange cross-sections. 50

985 2 Schematic wide-flange cross-section and mixed-dimension domains. 51

986 3 Schematic view of prototype frame and overview of Case Studies 2, 3, and 4. . . . 52

987 4 Details of the nonuniform torsion test, reproduced from Farwell and Galambos

988 (1969). 53

989 5 Schematic representations of the illustrative examples (extruded view of shell do-

990 mains shown). 54

991 6 Representations of the flange imperfection model. 55

992 7 Imperfections for a 5500 mm length W24X94 analysis model with a 20 % axial

993 load ratio, and (c) reference experimental results from Elkady and Lignos (2018a). 56

994 8 Comparison of applied torque versus twist angle for models of the Farwell and

995 Galambos (1969) test. 57

996 9 Comparisons of the von Mises equivalent stress (units of MPa) for the interface

997 shell elements in the nonuniform torsion models at $M_z = 11.25$ kN-m. 58

998 10 Iteration count for the nonuniform torsion test. 59

999 11 Comparisons of the DBBW overall subassembly behavior. Test Data retrieved from

1000 Engelhardt et al. (2000). 60

1001 12 Comparison of post-test deformed shapes from the DBBW subassembly. Test Data

1002 photo used with permission from Engelhardt et al. (2000). 61

1003 13 Comparisons of the DBBW panel zone behavior. Test Data retrieved from Engel-

1004 hardt et al. (2000). 62

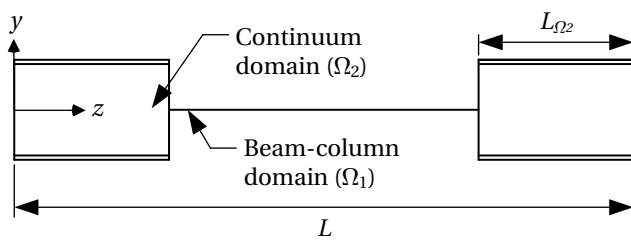
1005 14 Computational resource requirements for Case Studies 2, 3, and 4 normalized by

1006 the Full-shell values. 63

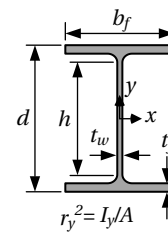
1007 15 Results from the W24X136 quasi-static analyses. Test Data retrieved from Elkady

1008 and Lignos (2018a). 64

1009 16 Deformed shapes from the W24X146 quasi-static analyses at 11 % SDR. von Mises
1010 equivalent stress profile shown on the deformed shape, red regions indicate yielding.
1011 Test Data photo used with permission from Elkady and Lignos (2018a). 65
1012 17 Results from the W24X94 column nonlinear response history analyses. 66
1013 18 Deformed shapes from the W24X94 column nonlinear response history analyses
1014 at $t = 4.5$ s. von Mises equivalent stress profile shown on the deformed shape, red
1015 regions indicate yielding. 67



(a) Mixed-dimension component macro model



(b) Wide-flange cross-section

Fig. 1. Mixed-dimension component macro model concept for wide-flange cross-sections.

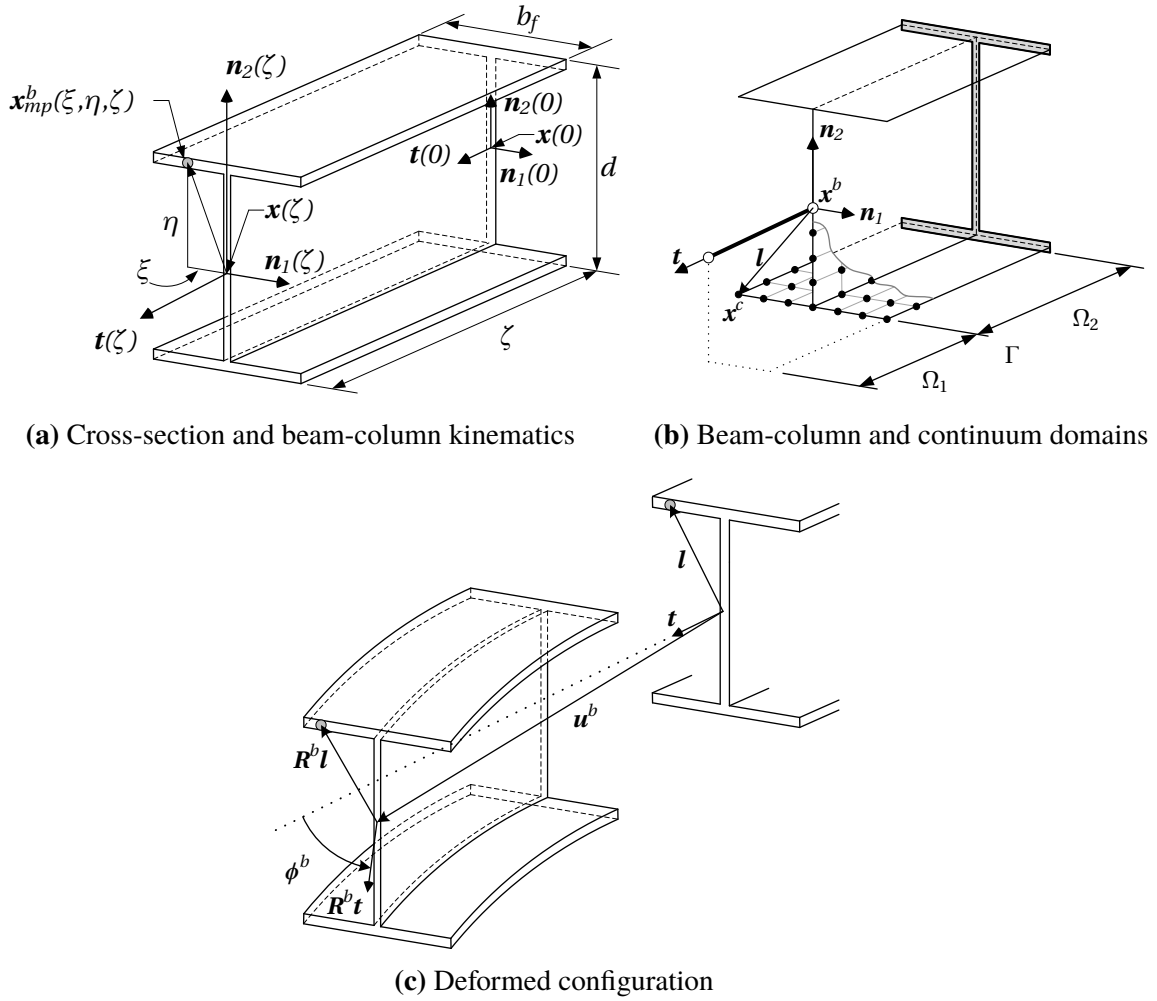


Fig. 2. Schematic wide-flange cross-section and mixed-dimension domains.

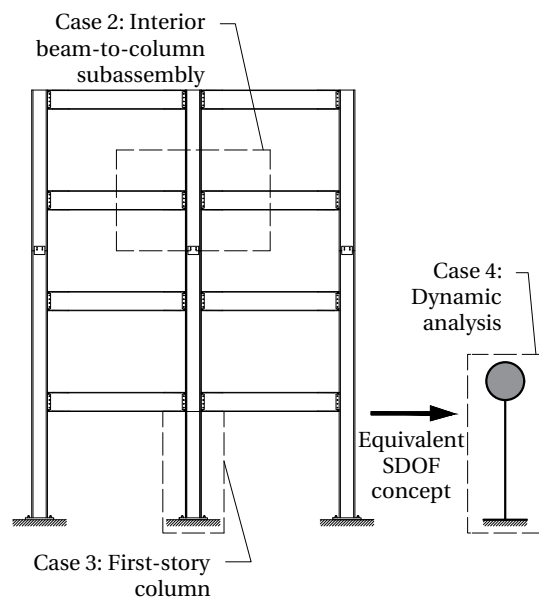


Fig. 3. Schematic view of prototype frame and overview of Case Studies 2, 3, and 4.

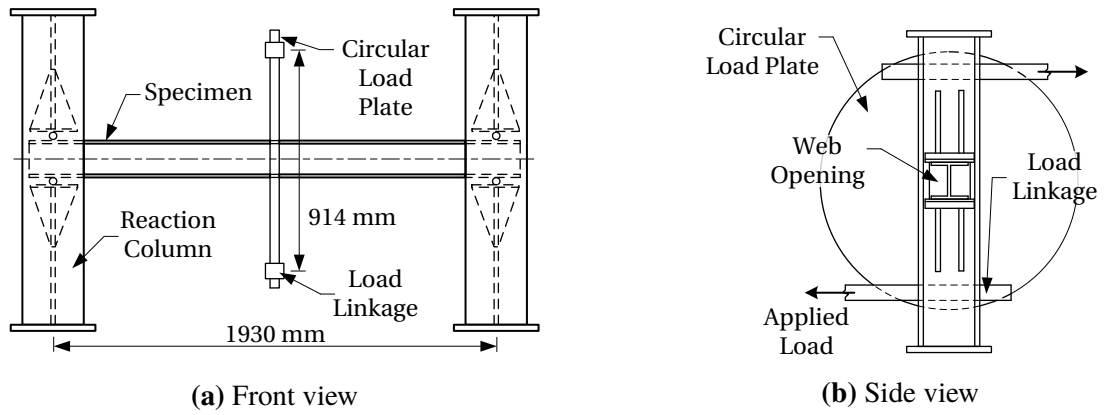


Fig. 4. Details of the nonuniform torsion test, reproduced from Farwell and Galambos (1969).

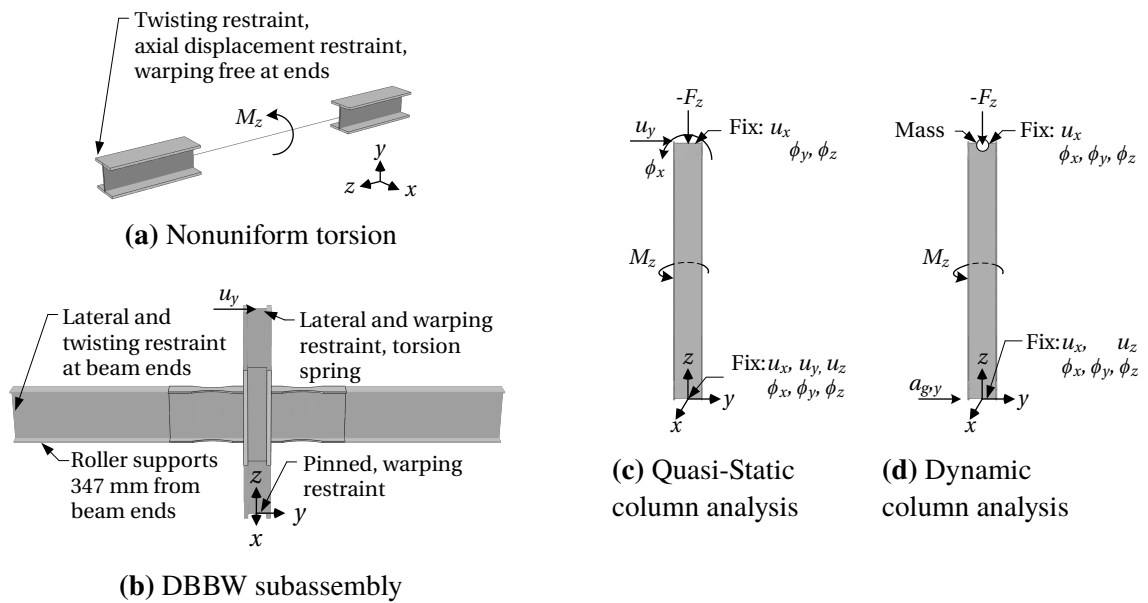
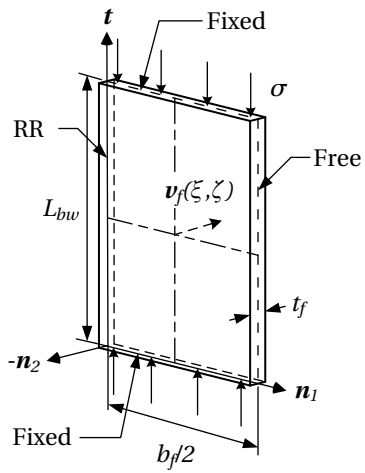
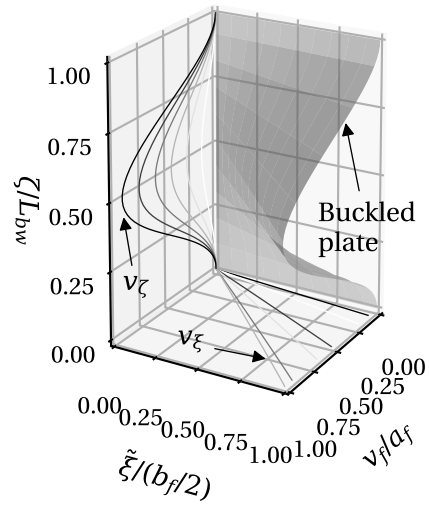


Fig. 5. Schematic representations of the illustrative examples (extruded view of shell domains shown).

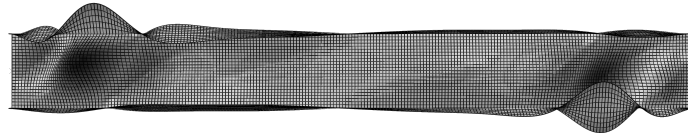


(a) Flange plate idealization

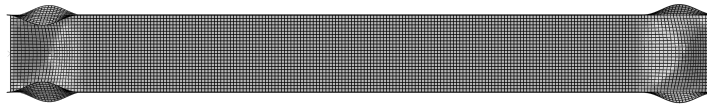


(b) Flange imperfection visualization

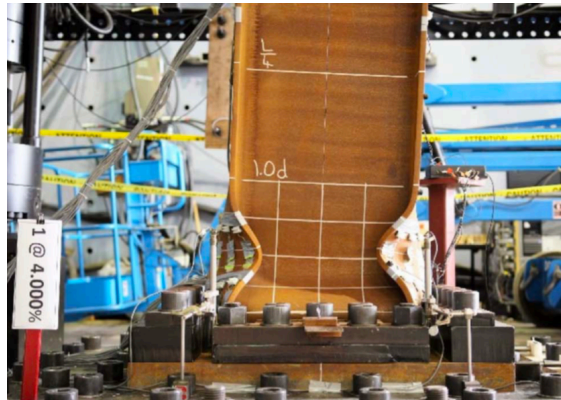
Fig. 6. Representations of the flange imperfection model.



(a) Selected local buckling mode, eigenvalue analysis

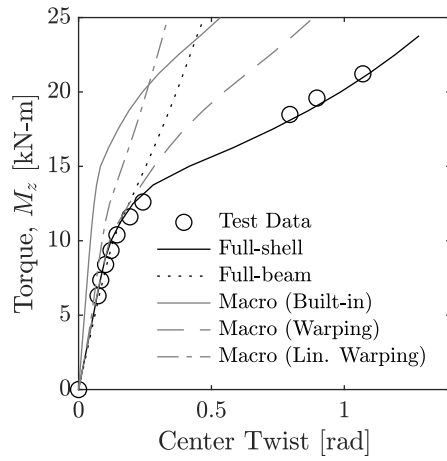


(b) Local imperfections applied to the model (scaled 100x)

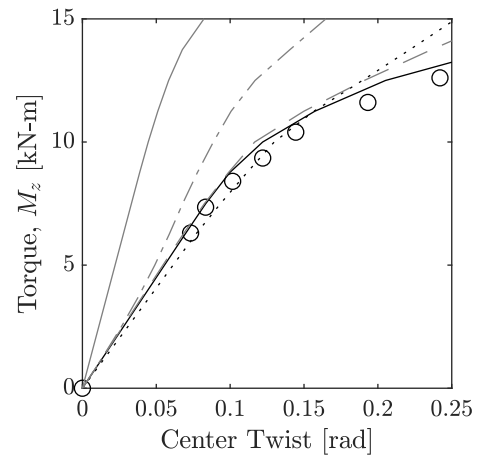


(c) Local buckling of a W24X84 (4 %SDR)

Fig. 7. Imperfections for a 5500 mm length W24X94 analysis model with a 20 % axial load ratio, and (c) reference experimental results from Elkady and Lignos (2018a).

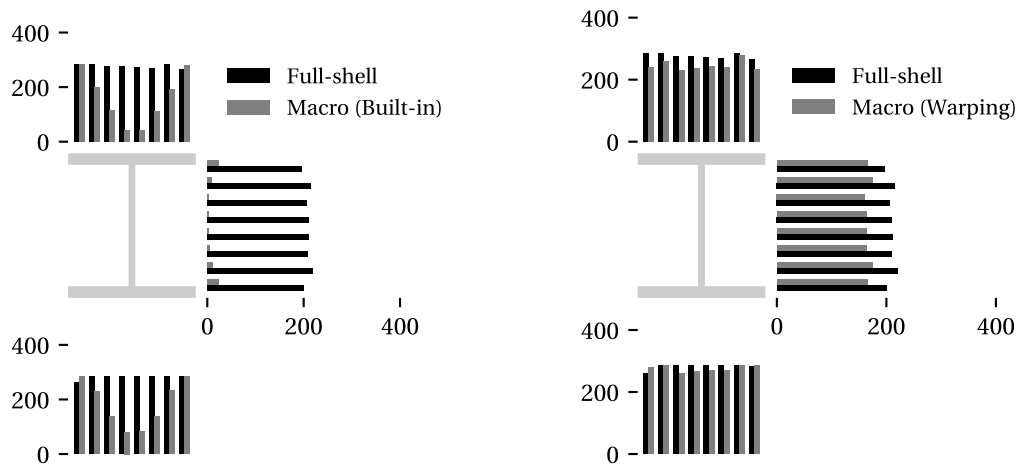


(a) Full loading history



(b) Zoom on initial loading

Fig. 8. Comparison of applied torque versus twist angle for models of the Farwell and Galambos (1969) test.



(a) Full-shell and Macro (Built-in) models

(b) Full-shell and Macro (Warping) models

Fig. 9. Comparisons of the von Mises equivalent stress (units of MPa) for the interface shell elements in the nonuniform torsion models at $M_z = 11.25$ kN-m.

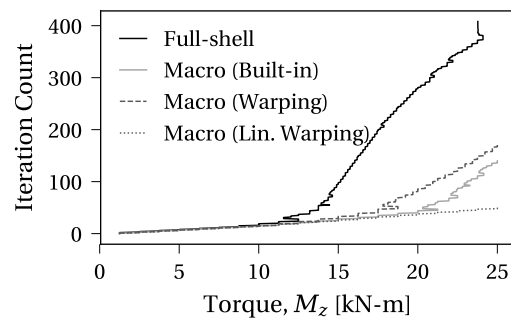
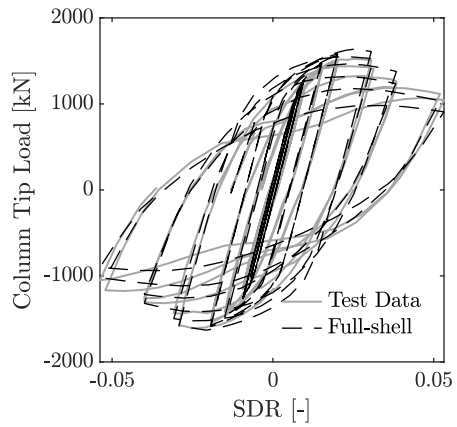
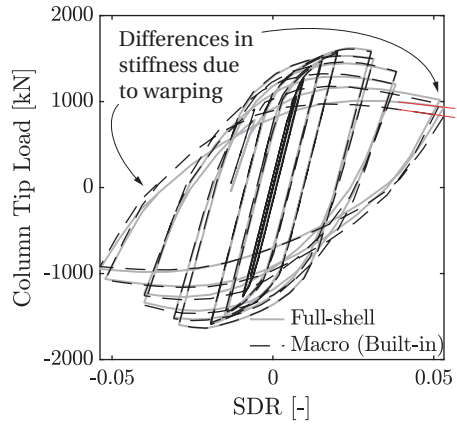


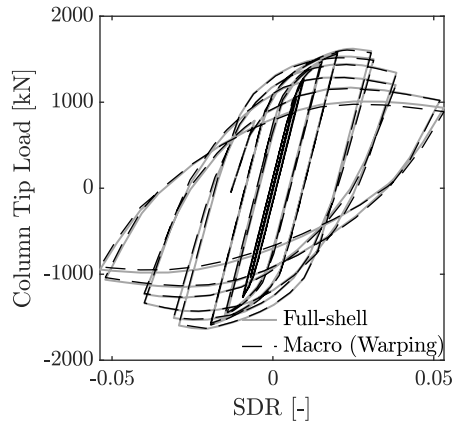
Fig. 10. Iteration count for the nonuniform torsion test.



(a) Test and Full-shell model

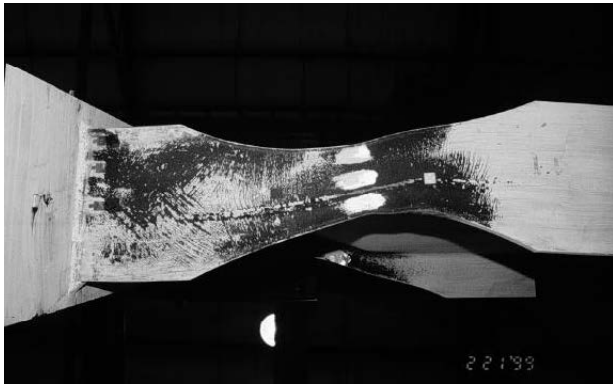


(b) Full-shell and Macro (Built-in) models

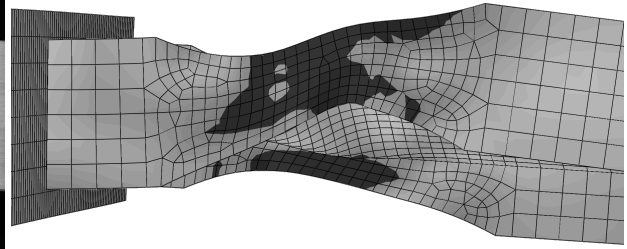


(c) Full-shell and Macro (Warping) models

Fig. 11. Comparisons of the DBBW overall subassembly behavior. Test Data retrieved from Engelhardt et al. (2000).

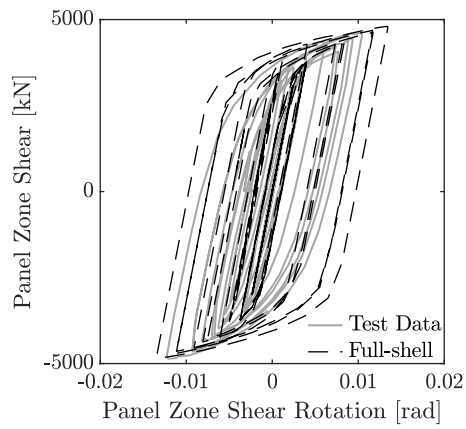


(a) Test Data

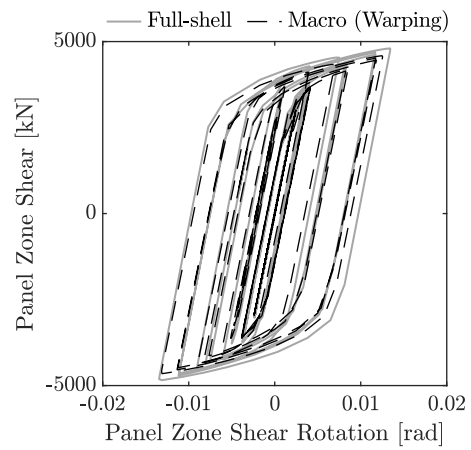


(b) Full-shell model

Fig. 12. Comparison of post-test deformed shapes from the DBBW subassembly. Test Data photo used with permission from Engelhardt et al. (2000).



(a) Test and Full-shell model



(b) Full-shell and Macro (Warping) models

Fig. 13. Comparisons of the DBBW panel zone behavior. Test Data retrieved from Engelhardt et al. (2000).

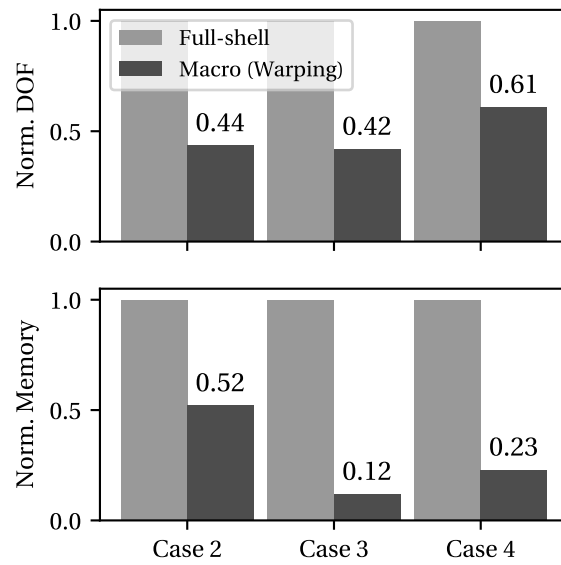


Fig. 14. Computational resource requirements for Case Studies 2, 3, and 4 normalized by the Full-shell values.

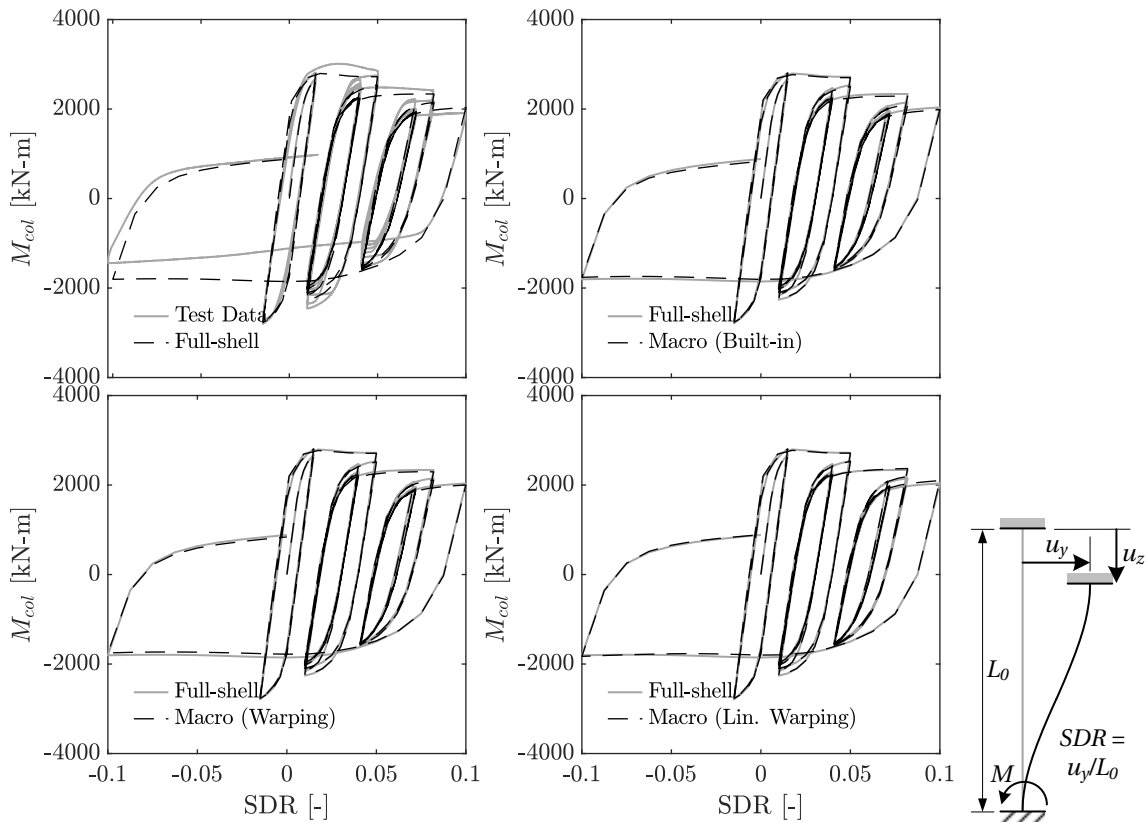


Fig. 15. Results from the W24X136 quasi-static analyses. Test Data retrieved from Elkady and Lignos (2018a).

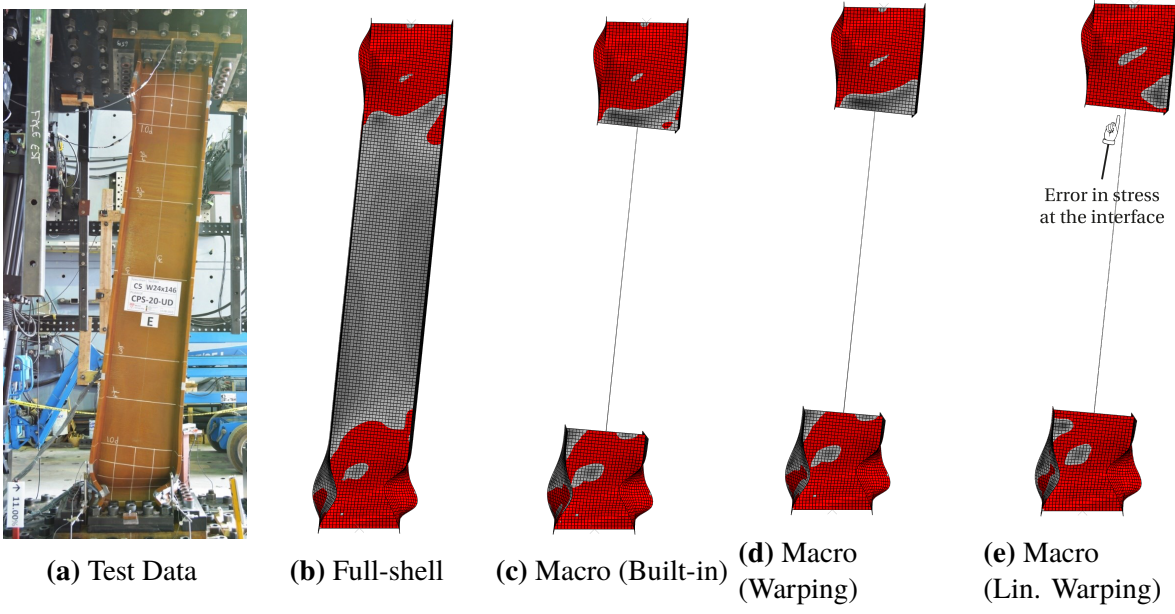


Fig. 16. Deformed shapes from the W24X146 quasi-static analyses at 11 % SDR. von Mises equivalent stress profile shown on the deformed shape, red regions indicate yielding. Test Data photo used with permission from Elkady and Lignos (2018a).

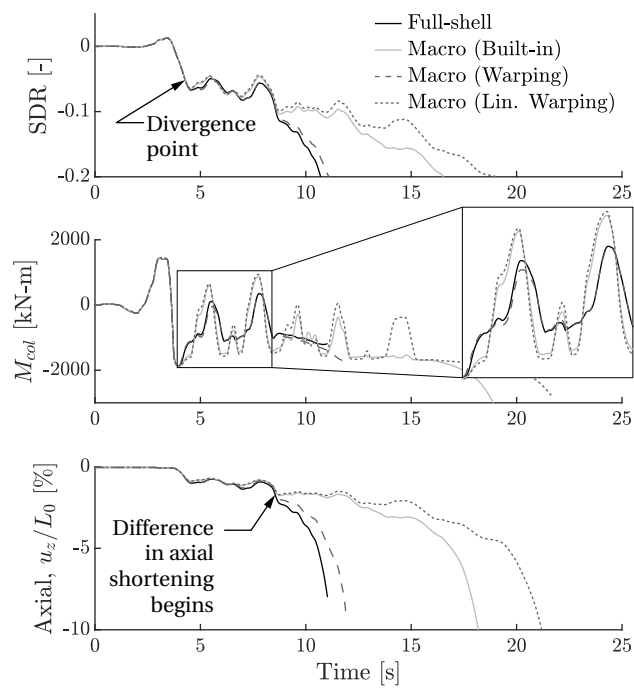


Fig. 17. Results from the W24X94 column nonlinear response history analyses.

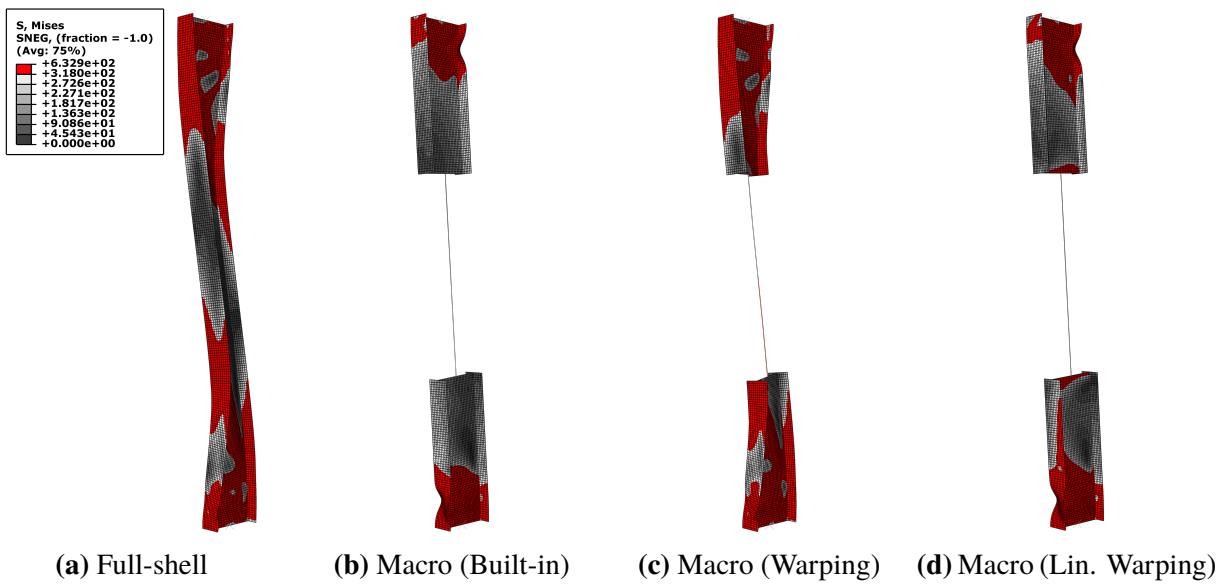


Fig. 18. Deformed shapes from the W24X94 column nonlinear response history analyses at $t = 4.5$ s. von Mises equivalent stress profile shown on the deformed shape, red regions indicate yielding.